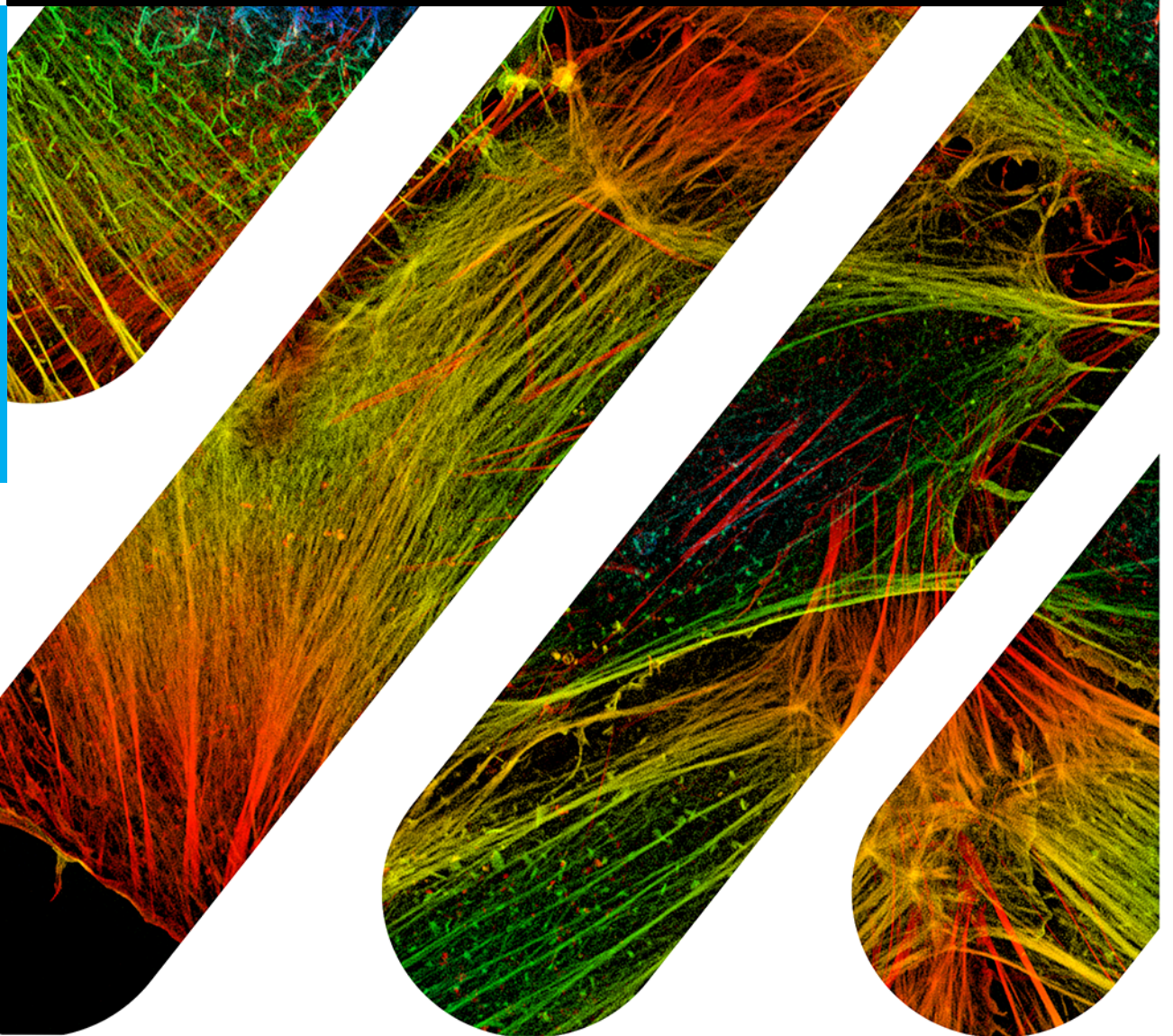


Joint Estimation of Object and Aberration for High Numerical Aperture Microscopy

Elia Trevisan



Joint Estimation of Object and Aberration for High Numerical Aperture Microscopy

MASTER OF SCIENCE THESIS

For the degree of Master of Science in Systems and Control at Delft
University of Technology

Elia Trevisan

August 27, 2020

Faculty of Mechanical, Maritime and Materials Engineering (3mE) · Delft University of
Technology

Abstract

Microscopic imaging has a resolution that is often far from the diffraction limit due to aberrations induced by the optics or by the sample itself. It is therefore of interest sensing these aberrations either directly or indirectly to improve image quality in post-processing or with adaptive optics. To avoid the use of extra hardware, several techniques are available to algorithmically retrieve aberrations in microscopy, but they often require images of an isolated point source, which is seldom a reasonable assumption as even single fluorescent beads often have a non negligible size. A different technique, known in literature joint estimation or phase diversity, was first developed by Gonsalves to estimate phase aberrations when imaging extended objects. In this master thesis we will derive a simple physical model that accounts for the vectorial nature of light and use it to expand the algorithms derived from Gonsalves seminal papers. We will show with numerical simulation that the effect of polarization is indeed non negligible when imaging through high-NA lenses, and therefore a vectorial model can substantially decrease model deviation and improve the quality of the estimates. The novel algorithm is thoroughly tested both in simulation and with experimental data.

Table of Contents

1	Introduction	1
2	Image Formation	3
2-1	Images as a Convolution	3
2-2	Scalar Diffraction Theory	4
2-2-1	Scalar PSF Model	4
2-3	Vectorial Diffraction Theory	7
2-3-1	Vectorial PSF Model	7
3	Phase Retrieval	11
3-1	Low Numerical Aperture	11
3-2	High Numerical Aperture	13
4	Joint Estimation	15
4-1	Joint Estimation of Object and Aberrations by Using Phase Diversity	16
4-2	Extension of Paxman's Joint Estimation to a Vectorial Model	17
4-3	Extension to Estimating Amplitude Aberrations	18
5	Simulations	21
5-1	Retrieval of Phase Only Aberrations	21
5-2	Retrieval of Amplitude and Phase Aberrations	23
5-3	Discontinuous Phase	27
5-4	Comparison Between Scalar and Vectorial Model	28
6	Experimental Data	31
7	Conclusions and Future Work	37

A Appendix: Scalar Diffraction Theory	39
A-1 Light as an Electromagnetic Radiation	39
A-1-1 The Scalar Wave	40
A-2 Wave propagation	40
A-2-1 Huygens-Fresnel Principle	40
A-2-2 Fresnel Diffraction	41
A-2-3 Fraunhofer Diffraction	42
B Appendix: Vectorial Diffraction Theory	43
B-1 Ray Tracing in Microscope Objectives	43
C Explicit Gradient	45
Bibliography	49
Glossary	53
List of Acronyms	53
List of Symbols	53

Chapter 1

Introduction

Knowledge of the aberration is extremely important in optical imaging as it allows for correction in real-time (e.g. with adaptive optics [1]) or in post-processing [2], as well as improving super-resolution techniques such as localization microscopy [3, 4].

In microscopy, aberrations have been estimated using wavefront sensing techniques [5], but these require additional hardware. A compact and flexible description of the imaging properties of a system is its pupil function, and this can be estimated algorithmically from intensity measures through phase retrieval [6]. Phase retrieval techniques, however, are often based on scalar diffraction theory, which is known to present significant model deviations for high-Numerical Aperture (NA) lenses [7, 8]. Only recently, a few algorithms for phase retrieval accounting for the vectorial nature of light appeared in literature [9, 10].

However, using either wavefront sensors or phase retrieval, we commonly require to image a point source (or at least to have an isolated point source in the object plane) [5, 11, 9], and this is often not the case. The solution to this has been to estimate the aberrations in the microscope first by imaging sub-resolution fluorescent beads, and then using this information for correction when imaging extended objects. This procedure also has its issues since, even in microscopy, the aberrations change over time as they might be induced by thermal effects or even the sample itself [12, 13]. Because of the aforementioned reasons, retrieving the pupil function directly when imaging the extended object would be highly desirable.

Phase retrieval techniques when imaging extended objects, also known as joint estimation, were studied in literature in the field of astronomy [14, 15, 16, 17], and for this reason were based on scalar diffraction theory. In that field, however, the aberrations are mostly due to turbulences in the atmosphere that quickly change over time and, therefore, the time-consuming algorithmic phase retrieval could not keep up. In microscopy instead, the aberrations have low bandwidth, and these algorithms become more suitable.

The main goal of this research would, therefore, be of adapting known joint estimation techniques [15] to a vectorial diffraction model more suitable for microscopy application [9], paving a new way for accurate estimates of the aberrations in microscopes when imaging extended objects.

Chapter 2

Image Formation

In this chapter we will provide a brief reasoning on how image formation can be formulated as a convolution against a kernel, where the latter is the impulse response of the optical system. This impulse response will first be derived according to the classical scalar diffraction theory. The derived model however, will show significant deviations from reality when used on systems with high-Numerical Aperture (NA). For this reason, a new impulse response will be derived specifically for microscopy accounting for the vectorial nature of light.

2-1 Images as a Convolution

By following the discussion given in chapter 2 of [18], we will define a system as a mathematical operator, $\mathcal{S}\{\cdot\}$, which operates on an input function to create an output function.

$$g_2(x_2, y_2) = \mathcal{S}\{g_1(x_1, y_1)\} \quad (2-1)$$

Using the sampling property of the delta function, one may rewrite the input g_1 , obtaining:

$$g_2(x_2, y_2) = \mathcal{S} \left\{ \iint_{-\infty}^{\infty} g_1(\xi, \eta) \delta(x_1 - \xi, y_1 - \eta) d\xi d\eta \right\} \quad (2-2)$$

In this expression $g_1(\xi, \eta)$ can be regarded as a number that multiplies the delta function and, if the system is linear (i.e. the operator $\mathcal{S}\{\cdot\}$ is linear), we obtain:

$$\begin{aligned} g_2(x_2, y_2) &= \iint_{-\infty}^{\infty} g_1(\xi, \eta) \mathcal{S}\{\delta(x_1 - \xi, y_1 - \eta)\} d\xi d\eta \\ &= \iint_{-\infty}^{\infty} g_1(\xi, \eta) h(x_2, y_2; \xi, \eta) d\xi d\eta \end{aligned} \quad (2-3)$$

Where $h(x_2, y_2; \xi, \eta) = \mathcal{S}\{\delta(x_1 - \xi, y_1 - \eta)\}$ is called impulse response of the system. The obtained expression shows us how a linear system is completely characterized by its responses to unit impulses. If, moreover, our optical systems is space-invariant, i.e. the impulse response depends only on the distances $(x - \xi)$ and $(y - \eta)$, we obtain the following:

$$\begin{aligned} g_2(x_2, y_2) &= \iint_{-\infty}^{\infty} g_1(\xi, \eta) h(x - \xi, y - \eta) d\xi d\eta \\ &= g_1 * h \end{aligned} \quad (2-4)$$

Which is a two-dimensional convolution between the input and the impulse response.

2-2 Scalar Diffraction Theory

We will now proceed to derive the impulse response according to scalar diffraction theory of an optical system composed of a single thin lens that images a monochromatic object. More details on scalar diffraction theory can be found in appendix A. Most of the information in this section has been taken from the book by Goodman [18], in which the reader will find a richer discussion of imaging systems in general.

2-2-1 Scalar PSF Model

Let us pose our attention on space-invariant linear optical systems. Under these conditions, we can in any case express the field in the image plane U_i (see Figure 2-1) by:

$$U_i(u, v) = \iint_{-\infty}^{\infty} h(u, v; \xi, \eta) U_o(\xi, \eta) d\xi d\eta \quad (2-5)$$

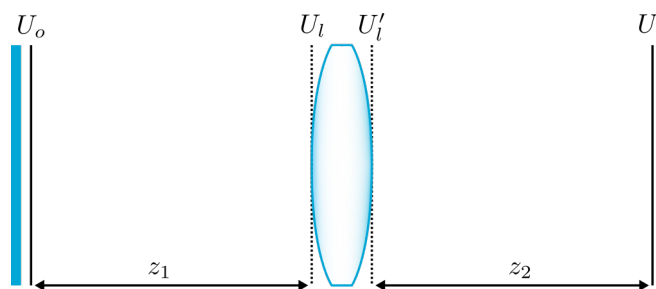


Figure 2-1: From left to right: the object field U_o , the field before the lens U_l , the field after the lens U'_l , the field on the image plane U_i .

So what is the impulse response of such a system? Let our object be a δ function (point source) at coordinates (ξ, η) . On the lens we will obtain a spherical wavefront, which paraxial approximation is:

$$U_l(x, y) = \frac{1}{i\lambda z_1} e^{i\frac{k}{2z_1}((x-\xi)^2 + (y-\eta)^2)} \quad (2-6)$$

After the lens of focal length f the field becomes:

$$U'_l(x, y) = U_l(x, y)P(x, y)e^{-i\frac{k}{2f}(x^2+y^2)} \quad (2-7)$$

Where $P(x, y) = \mathcal{X}e^{i\Phi}$ is the pupil function that, in general, not only describes the shape of the pupil (eg. taking value 1 inside the pupil and 0 outside), but might also include amplitude and phase aberrations. If we use Fresnel diffraction (eq. A-12) to account for propagation over the distance z_2 we obtain:

$$\begin{aligned} h(u, v; \xi, \eta) &= \frac{1}{i\lambda z_2} \iint_{-\infty}^{\infty} U'_l(x, y) e^{i\frac{k}{2z_2}((u-x)^2+(v-y)^2)} dx dy \\ &= \frac{1}{i\lambda^2 z_1 z_2} \iint_{-\infty}^{\infty} e^{i\frac{k}{2z_1}((x-\xi)^2+(y-\eta)^2)} P(x, y) e^{-i\frac{k}{2f}(x^2+y^2)} e^{i\frac{k}{2z_2}((u-x)^2+(v-y)^2)} dx dy \\ &= \frac{1}{i\lambda^2 z_1 z_2} e^{i\frac{k}{2z_2}(u^2+v^2)} e^{i\frac{k}{2z_1}(\xi^2+\eta^2)} \iint_{-\infty}^{\infty} P(x, y) e^{i\frac{k}{2}\left(\frac{1}{z_1}+\frac{1}{z_2}+\frac{1}{f}\right)(x^2+y^2)} \\ &\quad \times e^{ik\left(\left(\frac{\xi}{z_1}+\frac{u}{z_2}\right)x+\left(\frac{\eta}{z_1}+\frac{v}{z_2}\right)y\right)} dx dy \end{aligned} \quad (2-8)$$

We now have an expression for the impulse response that we could plug into the convolution integral to compute the image of any given object. However, further simplifications can be applied.

- The term $e^{i\frac{k}{2}\left(\frac{1}{z_1}+\frac{1}{z_2}+\frac{1}{f}\right)(x^2+y^2)}$ can be ignored if we enforce $\frac{1}{z_1} + \frac{1}{z_2} + \frac{1}{f} = 0$, also known as lens law.
- The term $e^{i\frac{k}{2z_2}(u^2+v^2)}$ can be ignored as it comes out of the convolution integral and, because of the nature of the camera sensors, we are only interested in the intensity.
- The term $e^{i\frac{k}{2z_1}(\xi^2+\eta^2)}$ can be reasonably approximated by $e^{i\frac{k}{2z_1}\left(\frac{u^2+v^2}{M^2}\right)}$ [18], where $M = -z_2/z_1$ is the magnification of the system, and consecutively dropped as we are only looking at intensities.

We finally obtain:

$$\begin{aligned} h(u, v; \xi, \eta) &= \frac{1}{\lambda^2 z_1 z_2} \iint_{-\infty}^{\infty} P(x, y) e^{ik\left(\left(\frac{\xi}{z_1}+\frac{u}{z_2}\right)x+\left(\frac{\eta}{z_1}+\frac{v}{z_2}\right)y\right)} dx dy \\ &= \frac{1}{\lambda^2 z_1 z_2} \iint_{-\infty}^{\infty} P(x, y) e^{i\frac{2\pi}{\lambda z_2}((u-M\xi)x+(v-M\eta)y)} dx dy \end{aligned} \quad (2-9)$$

Which, up to scaling $1/(\lambda z_1)$, is the Fraunhofer diffraction pattern of the lens aperture. We can now introduce the change of coordinates $\tilde{\xi} = M\xi$ and $\tilde{\eta} = M\eta$ and obtain an impulse response that only depends on the differences $u - \tilde{\xi}$ and $v - \tilde{\eta}$, that is:

$$h(u - \tilde{\xi}, v - \tilde{\eta}) = \frac{1}{\lambda^2 z_1 z_2} \iint_{-\infty}^{\infty} P(x, y) e^{-i\frac{2\pi}{\lambda z_2}((u-\tilde{\xi})x+(v-\tilde{\eta})y)} dx dy \quad (2-10)$$

We can introduce other normalized coordinates:

$$\tilde{x} = \frac{x}{\lambda z_2} \quad \tilde{y} = \frac{y}{\lambda z_2} \quad \tilde{h} = \frac{h}{|M|}$$

Then the object to image relationship as defined in equation (2-5) becomes:

$$\begin{aligned} U_i(u, v) &= \iint_{-\infty}^{\infty} \tilde{h}(u - \tilde{\xi}, v - \tilde{\eta}) \left(\frac{1}{|M|} U_o \left(\frac{\tilde{\xi}}{M}, \frac{\tilde{\eta}}{M} \right) \right) d\tilde{\xi} d\tilde{\eta} \\ &= \tilde{h}(u, v) \circledast U_g(u, v) \end{aligned} \quad (2-11)$$

where

$$U_g(u, v) = \frac{1}{|M|} U_o \left(\frac{u}{M}, \frac{v}{M} \right) \quad (2-12)$$

is the geometrical optics prediction of the image (if we would not have diffraction) and

$$\begin{aligned} \tilde{h}(u, v) &= \iint_{-\infty}^{\infty} P(\lambda z_2 \tilde{x}, \lambda z_2 \tilde{y}) e^{-i2\pi(u\tilde{x}+v\tilde{y})} d\tilde{x} d\tilde{y} \\ &= \mathcal{F}P(u, v) \end{aligned} \quad (2-13)$$

is the impulse response, where with \mathcal{F} we represent the Fourier Transform. In incoherent optical systems, it is more common to talk about the intensity I of such impulse response, which in optics is called Point Spread Function (PSF), that is:

$$h_{I,s} = |\mathcal{F}(P)|^2 \quad (2-14)$$

where the subscripts I and s stand for intensity and scalar respectively, as we have derived this PSF using scalar diffraction theory.

2-3 Vectorial Diffraction Theory

The resolution of an optical system, i.e. the minimum distance r between two point sources such that they can be distinguished in their image, as it can be seen in [19] is given by:

$$r = \frac{1.22\lambda}{2n\sin\theta} = \frac{0.61\lambda}{\text{NA}} \quad (2-15)$$

This formula clearly suggests that to improve resolution of an optical system we can either use light with a shorter wavelength or increase the NA of the system.

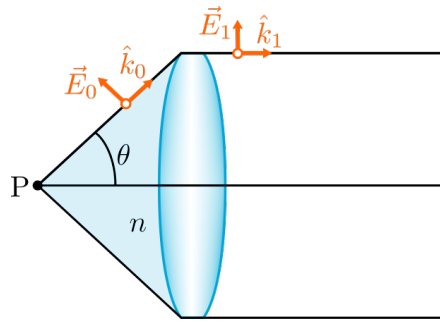


Figure 2-2: Bending of the propagation (\hat{k}) and field (\vec{E}) vectors through a high-NA lens.

The numerical aperture is given by $\text{NA} = ns\sin\theta$, where n is the refractive index of the medium and θ is the maximum semi-angle of the cone of light that can enter or exit the lens. In Figure 2-2, we see how a high-NA optical system receives a large cone of light from the point object. However, this also introduces a large bending in the propagation of the light rays, as well as in their polarization. In high-NA imaging systems ($\text{NA} \geq 0.6$) this phenomenon introduces non-negligible model deviation from scalar diffraction theory, where polarization and propagation vectors are neglected.

The famous solution to diffraction accounting the whole vectorial field was given by Wolf [20] and then expanded in the work of Richards and Wolf [7], where they demonstrated how a linearly polarized beam of light focusing through a high-NA lens produces a pattern that greatly differs from the regular Airy disk, as the time-averaged electric energy density (which is what is detected by a common sensor) loses its radial symmetry.

In the context of microscopy, it was demonstrated that when imaging a self-luminous, unpolarized, point object through a microscope with an high-NA objective lens, scalar diffraction theory overestimates the resolution of the microscope, predicting a spot due to diffraction that is smaller than the one predicted by vectorial diffraction [8]. This phenomenon would degrade the performances of a phase retrieval algorithm that does not account for the vectorial nature of light and, for this reason, we pursue a more accurate model that accounts for the bending of the rays and the polarization of the field.

2-3-1 Vectorial PSF Model

The scope of this section is not to derive rigorous computations of vectorial diffraction but instead tries to derive an approximated model of a generic microscope accounting for the

effects of polarization, such that it can be easily implemented in phase retrieval algorithms to improve their accuracy. We will follow a reasoning similar to the one in [8] but using Jones matrices to describe the bending of the rays.

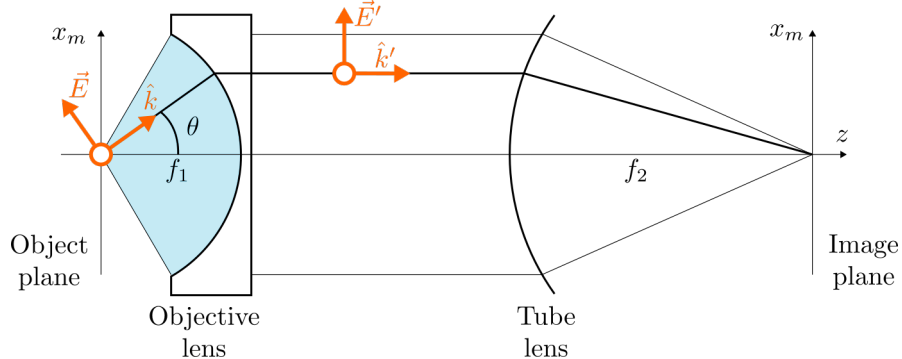


Figure 2-3: Approximated model of a microscope with negligible ray bending in the tube lens.

In Figure 2-3 we can see how the microscope is formed by two (groups of) lenses: the objective lens and the tube lens. The objective lens is the one with the high-NA, while the tube lens usually has a long focal length, and the depolarization caused by the latter is often negligible. In our model, a single fluorescent dipole is being imaged. Such a dipole creates an electric field given by: [21]

$$\vec{E} = (\hat{k} \times \vec{p}) \times \hat{k} \quad (2-16)$$

where multiplicative constant terms have been neglected, \hat{k} is a unit vector expressing the direction of propagation of the ray and \vec{p} is the electric dipolar moment. The symbol \times , instead, represents the cross product. The electric dipolar moment can be decomposed in its three components p_x , p_y and p_z . If we also decompose the propagation vector \hat{k} in its three components we can rewrite the field as:

$$\begin{aligned} \vec{E} = & [(k_z p_x - k_x p_z) k_z - (k_x p_y - k_y p_x) k_y] \hat{x} + [(k_x p_y - k_y p_x) k_x - (k_y p_z - k_z p_y) k_z] \hat{y} \\ & + [(k_y p_z - k_z p_y) k_y - (k_z p_x - k_x p_z) k_x] \hat{z} \end{aligned} \quad (2-17)$$

where \hat{x} , \hat{y} , and \hat{z} are, respectively, the unit vectors in the direction of the x , y , and z axes. We could also show the field produced by the single components of the dipole oriented in x , y and z respectively, that is:

$$\begin{aligned} \vec{E}_x &= p_x [(k_z^2 + k_y^2) \hat{x} - k_y k_x \hat{y} - k_z k_x \hat{z}] \\ \vec{E}_y &= p_y [-k_x k_y \hat{x} + (k_x^2 + k_z^2) \hat{y} - k_z k_y \hat{z}] \\ \vec{E}_z &= p_z [-k_x k_z \hat{x} - k_y k_z \hat{y} + (k_x^2 + k_y^2) \hat{z}] \end{aligned} \quad (2-18)$$

When the dipole is freely rotating, we have that p_x , p_y , and p_z are uncorrelated. Therefore, if we want to look at the time-averaged intensity of the electric field we can either do it by taking the magnitude of the field as expressed in eq. (2-17), or by summing the intensities of the fields produced by each of the dipole components given in eq. (2-18).

As we are now able to describe (up to constant multiplicative terms) the electric field before the objective lens, we now pose our attention to what happens after the objective lens.

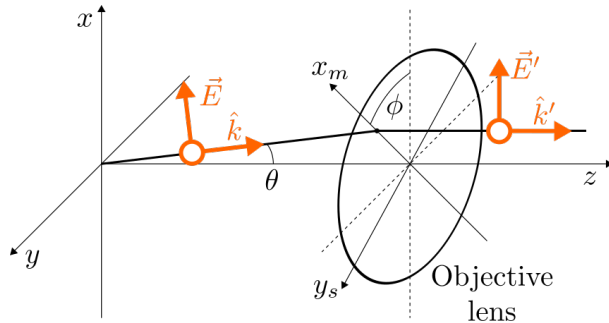


Figure 2-4: Diagram of the spherical coordinates used in the Jones matrices.

First, we start by describing the unit vector \hat{k} as function of the angles ϕ and θ as illustrated in Figure 2-4, that is:

$$\hat{k} = [\cos \phi \sin \theta, \sin \phi \sin \theta, \cos \theta]^T \quad (2-19)$$

We can then also describe all the components of the electric field as functions of those angles:

$$\begin{aligned} \vec{E}_x &= p_x [\cos^2 \theta + \sin^2 \phi \sin^2 \theta, -\sin^2 \theta \cos \phi \sin \theta, -\cos \phi \sin \theta \cos \theta]^T \\ \vec{E}_y &= p_y [-\sin^2 \theta \cos \phi \sin \phi, \cos^2 \phi \sin^2 \theta + \cos^2 \theta, -\sin \phi \sin \theta \cos \theta]^T \\ \vec{E}_z &= p_z [-\cos \phi \cos \theta \sin \theta, -\sin \phi \cos \theta \sin \theta, \sin^2 \theta]^T \end{aligned} \quad (2-20)$$

According to the 3×3 Jones matrices formalism for vectorial ray tracing [22] we can describe the vectorial field after the lens as a sequence of three rotations:

$$\vec{E}' = \mathbb{R}_z^{-1}(\phi) \mathbb{L}(-\theta) \mathbb{R}_z(\phi) \vec{E} \quad (2-21)$$

where we are first performing a coordinate rotation to express the field in its sagittal (y_s) and meridional (x_m) components, then we perform the ray refraction, and ultimately we perform the inverse coordinate rotation to return to the initial coordinate system. We can apply these rotations to the fields produced by each of the dipolar moment components and obtain:

$$\begin{aligned} \vec{E}'_x &= p_x \left[\underbrace{\sin^2 \phi + \cos^2 \phi \cos \theta}_{E_{xx}}, \underbrace{\cos \theta \cos \phi \sin \phi - \cos \phi \sin \phi}_{E_{xy}}, 0 \right]^T \\ \vec{E}'_y &= p_y \left[\underbrace{\cos \phi \sin \phi \cos \theta - \cos \phi \sin \phi}_{E_{yx}}, \underbrace{\sin^2 \phi \cos \theta + \cos^2 \phi}_{E_{yy}}, 0 \right]^T \\ \vec{E}'_z &= p_z \left[\underbrace{-\sin \theta \cos \phi}_{E_{zx}}, \underbrace{-\sin \theta \sin \phi}_{E_{zy}}, 0 \right]^T \end{aligned} \quad (2-22)$$

As we would expect, after the objective lens none of the fields shows a z component, as each ray is propagating parallel to the z axis. The under braced terms, e.g. E_{xy} , should be read as the y -polarized field behind the objective lens produced by the x component of the dipolar moment. We can express all these terms as function of their propagation vector \hat{k} before the

lens and obtain:

$$\begin{aligned} E_{xx} &= 1 - \frac{k_x^2}{1 + k_z}, & E_{xy} &= -\frac{k_x k_y}{1 + k_z} \\ E_{yx} &= -\frac{k_x k_y}{1 + k_z}, & E_{yy} &= 1 - \frac{k_y^2}{1 + k_z} \\ E_{zx} &= -k_x & E_{zy} &= -k_y \end{aligned} \quad (2-23)$$

The detailed computations can be found in Appendix B-1. The terms we have just found turn out to be exactly the coefficients derived by Mansuripur [23, 24], although he computed them for a linearly polarized collimated beam focusing through a high-NA lens.

What is now the intensity of the diffraction pattern measured at the focal plane of the low-NA tube lens? As we mentioned earlier, the components of the dipolar momentum p_x , p_y and p_z are uncorrelated, and therefore the intensity of the diffraction pattern can be computed as the sum of the intensities produced by each of those components.

The fields produced by each component of the dipole can be further separated into two scalar sub-components, one x -polarized and one y -polarized, as seen in eq. (2-22). According to the Fresnel-Arago laws [25], two fields with orthogonal polarization do not produce interference fringes, allowing us to compute the intensity as the sum of the diffraction patterns of each scalar sub-component.

Given the low-NA of the tube lens, the intensity of the diffraction pattern of each scalar sub-component of the field is given by the magnitude of the Fourier Transform of such sub-component multiplied by a pupil function P , the latter describing the finite size of the aperture and eventually also amplitude and phase aberration in the optical system. By this reasoning, the intensity at the focal plane can be computed as:

$$h_{I,v} = \sum_{cc} |\mathcal{F}(E_{cc} \cdot P)|^2 \quad (2-24)$$

Where constant multiplicative terms have been dropped and the index cc stands for the six pairs of coordinate indices xx , xy , yx , yy , zx , and zy . The subscript v , instead, stands for vectorial, as this PSF has been derived accounting for the vectorial nature of light.

Chapter 3

Phase Retrieval

In physics, the phase problem reduces to estimating the phase of a complex vector when a sensor can only record its intensity.

$$r = |x|^2, \quad x \in \mathbb{C}^K \quad (3-1)$$

As this clearly has infinite solutions, the problem is usually approached by taking intensity measurements of several function of x , and solving what is called the feasibility problem. Let us present a simple example where only two of such measurements are taken:

$$\begin{aligned} \text{given } & r_A = |x|^2 \\ & r_B = |Hx|^2 \\ \text{find } & x \in C_A \cap \{x : Hx \in C_B\} \end{aligned} \quad (3-2)$$

where H is a propagation operator, and C_i with $i = A, B$ is the set of complex valued vectors with squared modulus r_i , i.e. $C_i = \{y \in \mathbb{C}^K, |y|^2 = r_i\}$.

Several classes of methods have been developed to solve such a problem, of which the most popular one seems to be in the class of alternating projections methods. The interested reader might find different solutions and applications in various famous surveys [26, 27]. In the rest of this chapter, we will present a brief review of the phase retrieval problem in optics. We will focus on the retrieval of pupil functions and see how these algorithms have been recently expanded to more complicated models such as the one shown in eq. (2-24).

3-1 Low Numerical Aperture

The seminal paper in phase retrieval in optical systems was written by Gerchberg and Saxton [6], where they developed an alternating projection algorithm to estimate the object field when the intensity was measured directly at the object plane and its diffraction plane. This problem is the same as the one presented in eq. (3-2), where the propagation operator is the

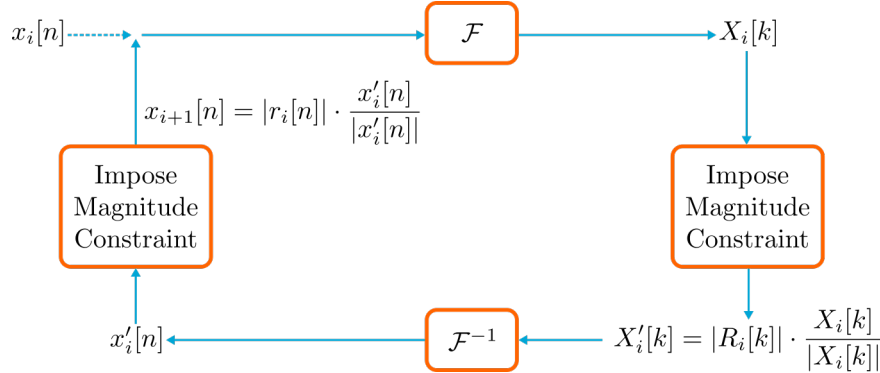


Figure 3-1: The block diagram of the Gerchberg and Saxton (GS) algorithm.

Fourier transform. A schematic of this iterative algorithm is given in Figure 3-1, where we can see how we iteratively project between the sets C_A and C_B by enforcing the magnitude constraint.

Fienup instead developed a modified version of the algorithm for the case in which the intensity measurement at the object plane is not available and therefore the magnitude constraint is replaced by other constraints, such as non-negativity or a known support [26, 28]. One of the most commonly used variations of the Fienup's algorithms, name the Hybrid Input-Output (HIO) algorithm, is essentially the same as the GS algorithm where the imposition of the object-space magnitude constraint is replaced by applying a correction:

$$x_{i+1}[n] = \begin{cases} x'_i[n], & n \notin \gamma \\ x_i[n] - \beta x'_i[n], & n \in \gamma \end{cases} \quad (3-3)$$

with γ being the set of indices for which $x'_i[n]$ violates some known constraint and β some small parameter. A schematic of this algorithm can be seen in Figure 3-2.

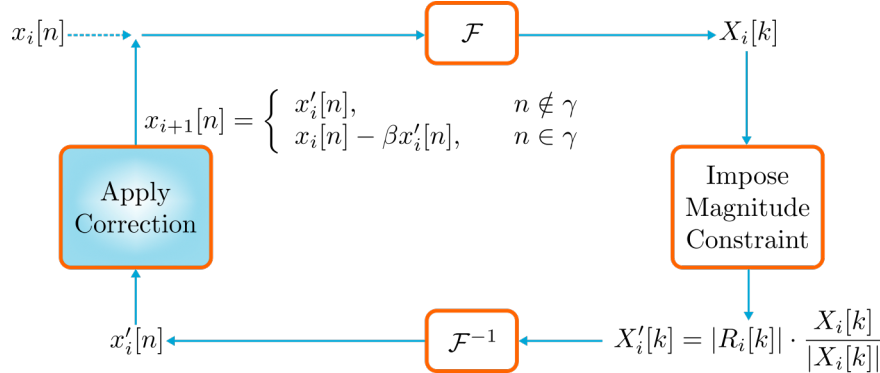


Figure 3-2: The block diagram of Fienup's HIO algorithm.

Direct application of both the GS algorithm and the HIO algorithm can be found in scanning Coherent Diffraction Imaging (CDI) [29] or crystallography [30]. More recently these algorithms have been slightly adapted to estimate pupil functions in microscopy, as in the work of Hanser et al. [31]. In this algorithm, several intensity images are taken around the focal plane, a technique that takes the name of phase diversity. We will express the pupil function

to be retrieved as $P = \mathcal{X}e^{j\Phi}$, with $\mathcal{X} \in \mathbb{R}^{n \times n}$ and $\Phi \in \mathbb{R}^{n \times n}$. We will then record several images at distances z_d from the focal plane, that will give rise to a defocus phase function $e^{i\phi_d}$ where $\phi_d = \frac{2\pi}{\lambda}z_d k_z$ with $k_z = \sqrt{1 - k_x^2 - k_y^2}$ the z -component of the unit propagation vector. According to scalar diffraction theory, when imaging a monochromatic point object we will record an intensity for each diversity image d given by:

$$r_d = |\mathcal{F}(\mathcal{X}e^{i(\Phi+\phi_d)})|^2 + \omega_d \quad (d = 1, \dots, D) \quad (3-4)$$

where $\omega_d \in \mathbb{R}^{n \times n}$ represents noise.

Algorithm 1: Scalar PSF model-based alternating minimization

N - maximum number of iteration;

τ - tolerance threshold;

$k = 0$ - current iteration number;

x^0 - initial guess for $\mathcal{X}e^{i\Phi}$;

while $k \leq N$ and $\|x^k - x^{k+1}\|_F < \tau$ **do**

$$X_d^k = \mathcal{F}(x^k e^{i\phi_d});$$

$$Y_d^k = \frac{x_d^k}{|x_d^k|} \sqrt{r_d};$$

$$y_d^k = e^{-i\phi_d} \mathcal{F}^{-1}(Y_d^k);$$

$$x^{k+1} = (\sum_{d=1}^m y_d^k)/m;$$

end

Result: $\hat{\Phi} = \arg(x^{end})$ - the estimated phase. $\hat{\mathcal{X}} = |x^{end}|$ - the estimated amplitude.

An interesting visual schematic of this algorithm can be seen in later work [12].

All of the algorithms above involve a "pure projection", meaning that the estimated magnitude is simply substituted by the measured one. However, when the measured intensities also involve noise, these projections can take into account the noise statistics to improve convergence by making use of proximity operators [32].

3-2 High Numerical Aperture

In the previous section, we have seen how alternating projection algorithms have evolved and have been used to retrieve the pupil function of a microscope but always using models derived from the scalar diffraction theory. A recent publication from Nguyen et al. [9] uses instead the model we derived in eq. (2-24) and, although in a more involved manner, follows the same idea of phase diversity and alternating projections. Given the same premises of Algorithm 1, we will report here the Vectorial Alternating Minimization (VAM) algorithm developed in [9] for simplicity of the reader. Now, our recorded image is given by:

$$r_d = \sum_{cc} |\mathcal{F}(E_{cc}\mathcal{X}e^{i(\Phi+\phi_d)})|^2 + \omega_d \quad (d = 1, \dots, D) \quad (3-5)$$

Algorithm 2: Vectorial PSF model-based alternating minimization (VAM)

N - maximum number of iteration;
 τ - tolerance threshold;
 $k = 0$ - current iteration number;
 Φ^0 - initial guess for Φ ;
 \mathcal{X}^0 - initial guess for \mathcal{X} ;

```

while  $k \leq N$  and  $\|I_d^k - I_d^{k+1}\|_F < \tau$  do
     $x_{cc}^k = E_{cc}\mathcal{X}^k e^{i\Phi^k};$ 
     $X_{cc,d}^k = \mathcal{F}(x_{cc}^k e^{i\phi_d});$ 
     $I_d^k = \sum_{cc} |X_{cc,d}^k|^2;$ 
     $Y_{cc,d}^k = \frac{X_{cc,d}^k}{I_d^k} \sqrt{r_d};$ 
     $y_{cc,d}^k = e^{-j\phi_d} \mathcal{F}^{-1}(Y_{cc,d}^k);$ 
     $\bar{y}_{cc}^k = (\sum_{d=1}^m y_{cc,d}^k)/m;$ 
     $\Phi^{k+1} = \arg(\sum_{cc} (E_{cc}\bar{y}_{cc}^k));$ 
     $\mathcal{X}^{k+1} = \frac{|\sum_{cc} E_{cc}\bar{y}_{cc}^k|}{\sum_{cc} |E_{cc}|^2};$ 
end
```

Result: $\hat{\Phi} = \Phi^{end}$ - the estimated phase. $\hat{\mathcal{X}} = \mathcal{X}^{end}$ - the estimated amplitude.

This algorithm was numerically proven to be more accurate than the Algorithm 1 for systems of high-Numerical Aperture (NA), once again showing that the previously derived vectorial model is more precise compared to the scalar one.

Chapter 4

Joint Estimation

In the previous chapters we have shown how it is possible to estimate amplitude and phase aberrations in low and high Numerical Aperture (NA) settings when recording directly the Point Spread Function (PSF) of a system, i.e. when imaging what is known as a point object. But what to do when we take images of an extended object? Given the linearity of optical systems and if, moreover, the system is isoplanatic, the recorded images can be expressed as a convolution between the object o and the PSF h_I , that is:

$$i = o \circledast h_I \quad (4-1)$$

If we take the Fourier transform the equation above, we will obtain:

$$I = O \cdot H \quad (4-2)$$

where H is called the Optical Transfer Function (OTF). The algorithmic retrieval of the original object o and the pupil function P from intensity images is known in literature as Joint Estimation. A good review of the current state of the art can be found in [33].

The basic idea comes from two seminal papers from Gonsalves [34, 14]. Let us now define as usual:

$$\begin{aligned} r_d &= o \circledast h_d + \omega_d \quad (d = 1, \dots, D) \\ r_d, o, h_d &\in \mathbb{R}_+^{n \times n} \end{aligned} \quad (4-3)$$

which, once Fourier transformed, becomes:

$$R_d = H_d \cdot O + \Omega_d \quad (4-4)$$

where:

$$H_d = \mathcal{F}(|\mathcal{F}(\mathcal{X}e^{i(\Phi+\phi_d)})|^2) \quad (4-5)$$

and where \mathcal{X} is a known amplitude of the pupil function, Φ is the unknown phase aberration and ϕ_d is the known phase diversity. We can parametrize the unknown Φ using a set of basis function ϕ_j as follows:

$$\Phi = \sum_{j=1}^J \alpha_j \Phi_j \quad (4-6)$$

where these basis functions could be Zernike polynomials or pixel-by-pixel Kronecker delta functions. If we had a metric to minimize with respect to the parameters α_j that does not depend on the object, we would have solved our problem. Gonsalves, assuming to have only two diversity images, used the metric:

$$E = \int (i_1(x) - \hat{o}(x) \circledast \hat{h}_1(x))^2 dx + \int (i_2(x) - \hat{o}(x) \circledast \hat{h}_2(x))^2 dx \quad (4-7)$$

of which minimization with respect to the object has the following closed form solution:

$$\hat{O}(u) = \frac{\hat{H}_1^*(u)I_1(u) + \hat{H}_2^*(u)I_2(u)}{|\hat{H}_1(u)|^2 + |\hat{H}_2(u)|^2} \quad (4-8)$$

where H^* is the complex conjugate of H . The object can now be substituted into the error metric, and the new object-independent metric can be minimized only with respect to the parameters α_j .

Other similar object-independent metrics have been developed in literature [17], but the one from Gonsalves and its derivations are by far the most popular ones.

4-1 Joint Estimation of Object and Aberrations by Using Phase Diversity

A very famous expansion of the Gonsalves error metric is the one developed by Paxman et al [15]. In this paper, they have not only expanded the algorithms to accept an arbitrary number of diversity images, but they have also justified the error metrics in a maximum likelihood fashion. As with the Gonsalves algorithm, they proceed by parametrizing the unknown phase with a set of basis functions as in (4-6), and they assume that the amplitude of the pupil function is known. To derive the error metric, they start by writing down the probability density for realizing a whole data set $\{r_d\}$ consisting of each recorded pixel x , given an object o and a set of parameters α . That is:

$$p(\{r_d\}, o, \alpha) = \prod_{d=1}^D \prod_x \frac{1}{\sqrt{2\pi\sigma_\omega^2}} e^{-\frac{(r_d - o \circledast h_d)^2}{2\sigma_\omega^2}} \quad (4-9)$$

which is true when the noise ω is assumed Gaussian. If we would be able to maximize such probability with respect to o and α we would estimate the object and aberrations that are most likely to have generated that data set. The easiest way to proceed is to take the logarithm of such probability density, dropping constant and scaling terms, and using a discrete version of Parseval's theorem to transform convolution in spatial domain into multiplication in the spatial frequency domain.

$$L(o, \alpha) = - \sum_{d=1}^D \sum_{u \in \mathcal{U}} |R_d(u) - O(u)H_d(u)|^2 \quad (4-10)$$

If we take the derivative of this log-likelihood functions with respect to the object we can find that the object that maximizes the likelihood is given by:

$$\hat{O}(u) = \begin{cases} \frac{\sum_{d=1}^m R_d(u)H_d^*(u)}{\sum_{l=1}^m |H_l(u)|^2} & u \in \mathcal{U}_1 \\ \hat{O}^*(-u) & u \in \mathcal{U}_0 \end{cases} \quad (4-11)$$

where \mathcal{U}_0 is the set of spatial frequencies at which all OTFs are zero values, and \mathcal{U}_1 is its complement. The object independent log-likelihood function is therefore derived by substituting the maximizing object into eq.(4-10), obtaining:

$$L_M(\alpha) = \sum_{u \in \mathcal{U}_1} \frac{|\sum_{d=1}^m R_d(u) H_d^*(u)|^2}{\sum_{l=1}^m |H_l^*(u)|^2} - \sum_{u \in \mathcal{U}_0} \sum_{k=1}^m |R_k(u)|^2 \quad (4-12)$$

This log-likelihood function, only dependent on the aberration parameter alpha, can be maximized, for example with gradient descent, by computing its analytical partial derivatives, that are:

$$\frac{\partial}{\partial \alpha_n} L_M = \sum_{u \in \mathcal{U}} \sum_{d=1}^m Z_d \frac{\partial}{\partial \alpha_n} H_d \quad (4-13)$$

where

$$Z_d = \begin{cases} \frac{\sum_l |H_l|^2 (\sum_k R_k H_k^*) R_d^* - |\sum_k D_k H_k^*|^2 H_d^*}{(\sum_l |H_l|^2)^2} & u \in \mathcal{U}_1 \\ 0 & u \in \mathcal{U}_0 \end{cases} \quad (4-14)$$

In the original paper [15] the explicit derivatives of the OTFs with respect to the aberration parameters were computed using the model given by scalar diffraction theory (eq. (4-5)), and the method was confirmed to be successful in retrieving phase aberrations when imaging extended objects.

4-2 Extension of Paxman's Joint Estimation to a Vectorial Model

In order to account for the polarization effects, we only need to compute the partial derivatives of the OTF with respect to each parameter α_n expressed using the vectorial model, i.e.:

$$H_d(u) = \mathcal{F}(\sum_{cc} |\mathcal{F}(E_{cc}(u)P_d(u))|^2), \quad P_d(u) = \mathcal{X}(u)e^{i(\sum_{j=1}^J \alpha_j \Phi_j(u) + \phi_d(u))} \quad (4-15)$$

We will report here only the main steps of the derivation, where all the details can be found in Appendix C. We would like to remind that the autocorrelation theorem tells us that:

$$\mathcal{F}(|g(x)|^2) = \iint_{-\infty}^{\infty} G(u')G^*(u' - u)du', \quad G(u) = \mathcal{F}g(u) \quad (4-16)$$

where with the asterisk * we represent the complex conjugate. In our case $g(x)$ is equal to $\mathcal{F}(E_{cc}(u)P_d(u))$ which, when Fourier transformed, becomes:

$$\mathcal{F}(\mathcal{F}(E_{cc}(u)P_d(u))) = E_{cc}(-u)P_d(-u) \quad (4-17)$$

We now have a way to rewrite our OTF. Given that all the signals are actually sampled (we have pixels instead of a continuous functions) we will use a discrete version of the autocorrelation theorem.

$$H_d(u) = \frac{1}{N^2} \sum_{cc} \sum_{u' \in \mathcal{U}} E_{cc}(-u')P_d(-u')E_{cc}(u - u')P_d^*(u - u') \quad (4-18)$$

The derivative of the vectorial OTF with respect to one of the parameters α_n can be computed as:

$$\frac{\partial}{\partial \alpha_n} H_d(u) = \frac{i}{N^2} \sum_{cc} \sum_{u' \in \mathcal{U}} \Phi_n(u') E_{cc}(u') [E_{cc}(u+u') P_d(u') P_d^*(u+u') \dots \\ \dots - E_{cc}(u'-u) P_d^*(u') P_d(u'-u)] \quad (4-19)$$

If we now input this into eq.(4-13) and simplify we obtain:

$$\frac{\partial}{\partial \alpha_n} L_M = -\frac{4}{N^2} \sum_{cc} \sum_{u' \in \mathcal{U}} \Phi_n(u') E_{cc}(u') \operatorname{Im} \left\{ \sum_{d=1}^m P_d(u') (Z_d^* \circledast (P_d^* E_{cc}))(u') \right\} \quad (4-20)$$

where the operator $\operatorname{Im}\{\}$ takes the imaginary part. These derivatives work with any kind of basis function Φ_n . In particular, for a pixel-wise estimate of the phase, we can take Φ_n to be a Kronecker delta function, i.e.:

$$\Phi_n(u) = \begin{cases} 1, & \text{for } u = u_n \\ 0, & \text{for } u \neq u_n \end{cases} \quad (4-21)$$

In this case, the partial derivative of the log-likelihood simplifies to:

$$\frac{\partial}{\partial \alpha_n} L_M = -\frac{4}{N^2} \sum_{cc} E_{cc}(u_n) \operatorname{Im} \left\{ \sum_{d=1}^m P_d(u_n) (Z_d^* \circledast (P_d^* E_{cc}))(u_n) \right\} \quad (4-22)$$

4-3 Extension to Estimating Amplitude Aberrations

The work of Paxman et al. [15] was later expanded to also estimate amplitude aberrations [16]. We would like to follow a similar approach for our algorithm based on the vectorial PSF model. The pupil function is then parametrized as:

$$P_d(u) = W(u) \sum_{k=1}^K f(\beta_k) \Theta_k(u) e^{i(\sum_{j=1}^J \alpha_j \Phi_j(u) + \phi_d(u))} \quad (4-23)$$

where $W(u)$ is a known support, Θ_k is a basis function and β_k is the corresponding parameter. The amplitude of the pupil function is always positive by convention. To avoid using constraints on the parameters β during the optimization we could truncate to zero parameters with a negative value at each iteration to project back into the desired space, but this would slow down the convergence of the algorithm [35]. Instead, we decide to use a monotonic, positive definite, and differentiable transformation function $f(\beta_n)$. A function that works well for our purpose is the hyperbola given by:

$$f(\beta_n) = 0.5 \left(\beta_n + \sqrt{\beta_n^2 + 1} \right) \quad (4-24)$$

As for the partial derivatives with respect to the parameters β_n , we end up with the following:

$$\begin{aligned} \frac{\partial}{\partial \beta_n} L_M &= \sum_{u \in \mathcal{U}} \sum_{d=1}^m Z_d \frac{\partial}{\partial \beta_n} H_d \\ &= -\frac{4}{N^2} f'(\beta_n) \sum_{cc} \sum_{u' \in \mathcal{U}} \Theta_n(u') E_{cc}(u') \operatorname{Re} \left\{ \sum_{d=1}^D e^{i\Phi_{tot}(u')} (Z_d^* \circledast (P_d^* E_{cc}))(u') \right\} \end{aligned} \quad (4-25)$$

where $\Phi_{tot}(u) = \sum_{j=1}^J \alpha_j \Phi_j(u) + \phi_d(u)$, the operator $Re\{\}$ takes the real part, and $f'(\beta_n)$ represents the first derivative of f with respect to β_n . If the basis function Θ_n are taken as Kronecker deltas then the partial derivatives simplify to:

$$\frac{\partial}{\partial \beta_n} L_M = -\frac{4}{N^2} f'(\beta_n) \sum_{cc} E_{cc}(u_n) Re \left\{ \sum_{d=1}^D e^{i\Phi_{tot}(u_n)} (Z_d^* \circledast (P_d^* E_{cc}))(u_n) \right\} \quad (4-26)$$

We now have an expression for the partial derivatives of the log-likelihood function with respect to both the amplitude and phase aberration parameters using our vectorial PSF model that accounts for the polarization of light.

Chapter 5

Simulations

To simulate the microscopic images we set a numerical aperture $NA = 1.49$, a refractive index $n = 1.518$, a wavelength of $\lambda = 640nm$, and a pixel size at the sample plane on $81.25nm$. Using these data we compute the radius of the support of the pupil according to the imaging model given by Hanser et al. [12] and the defocus phase function as:

$$\phi_d = 2\pi k_z z_d \quad (5-1)$$

where z_d is the defocus distance in meters.

5-1 Retrieval of Phase Only Aberrations

To generate the unknown phase aberration Φ we simply sum the Zernike polynomials with radial degree from 2 to 9 (52 Zernikes in total) using random multiplying coefficients. These coefficients are then normalized to have maximum phase aberration of 1.5π in absolute value. The piston term is not considered as it doesn't affect the image, while tip and tilt are also left out as they only shift the picture in the image plane. For the scope of this demonstration, we generate five images at different out-of-focus distances:

$$z = [-1.5 \ -0.75 \ 0 \ 0.75 \ 1.5] nm$$

We can now simply pick an object o and simulate the noisy recorded images using the vectorial Point Spread Function (PSF) model as follows:

$$\begin{aligned} i_d &= o \circledast h_d + \omega_d \\ h_d &= \sum_{cc} |\mathcal{F}(E_{cc} P_d)|^2 \\ P_d &= \mathcal{X} e^{i(\Phi + \phi_d)} \end{aligned} \quad (5-2)$$

In Figure 5-1 we can see the original object, the phase aberration and the amplitude which, in this case, is aberration free, i.e. of value 1 inside the support and 0 outside. In Figure 5-2

the five PSFs are presented, which are then convolved with the object to create the diversity images seen in Figure 5-3. Clearly, even when the image is on focus, many details of the original object are lost. Partly, as shown in eq. (2-15), this is due to high-frequencies being cut off by the limited aperture, but a significant loss of details also occurs due to the phase aberrations.

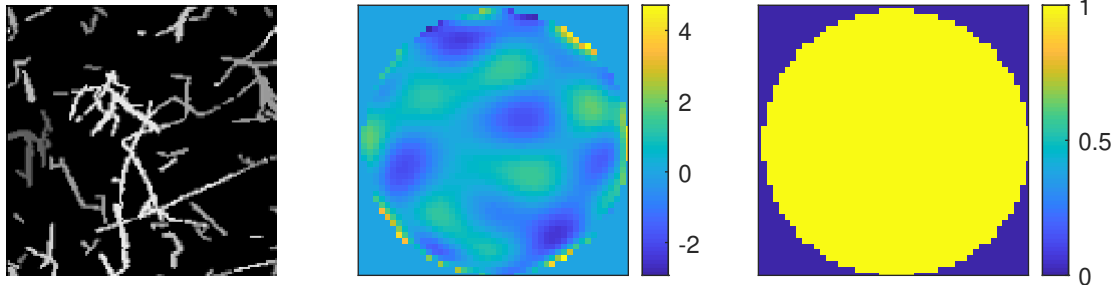


Figure 5-1: Data used to simulate diversity images with no amplitude aberrations. (Left) Original object o . (Middle) Phase aberration Φ . (Right) Amplitude X .

$$z_d = -1.5\text{e-}06\text{m} \quad z_d = -7.5\text{e-}07\text{m} \quad z_d = 0\text{m} \quad z_d = 7.5\text{e-}07\text{m} \quad z_d = 1.5\text{e-}06\text{m}$$

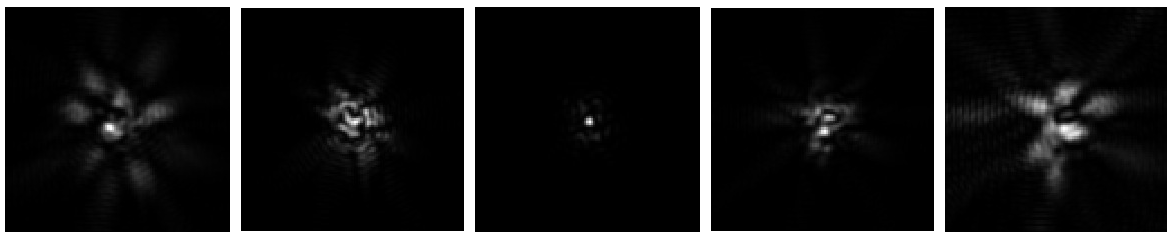


Figure 5-2: PSFs at different defocus distances using the data seen in Figure 5-1.

$$z_d = -1.5\text{e-}06\text{m} \quad z_d = -7.5\text{e-}07\text{m} \quad z_d = 0\text{m} \quad z_d = 7.5\text{e-}07\text{m} \quad z_d = 1.5\text{e-}06\text{m}$$

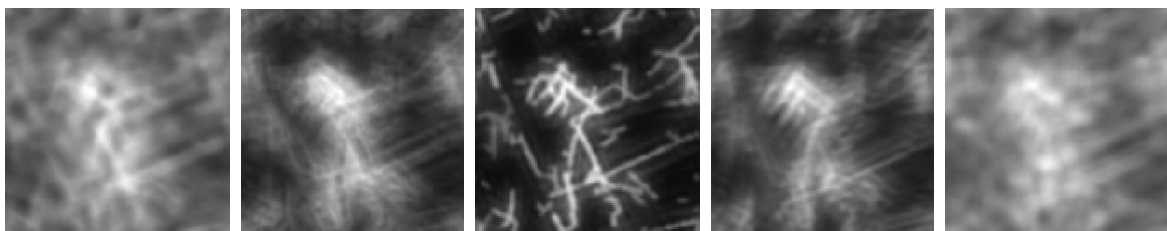


Figure 5-3: Aberrated images at different defocus distances using the data seen in Figure 5-1. Signal to Noise Ratio (SNR) 50dB.

We can now minimize the cost function given in eq. (4-10) with respect to the phase aberration parameters α to try and estimate the phase aberration from the diversity images assuming that the amplitude of the pupil function is known. At first, we choose the basis functions to also be the Zernike polynomials with radial degree from 2 to 9, the same basis functions that we used to create the phase aberrations in the first place. For the optimization, we opted for the conjugate gradient method given in the book Numerical Recipes in C [36] because of its ability to use gradient information during both the choice of search direction and line minimization, with no need to store a space-greedy Hessian. The estimated phase, shown in

Figure 5-4, is compared to the original one by creating a residual and computing the relative Root Mean Square (RMS) error as $\|\hat{\Phi} - \Phi\|_F / \|\Phi\|_F$, where $\hat{\Phi}$ is the estimated phase. From the figure we can conclude that the phase is almost perfectly estimated, having a relative RMS error of only 0.0003. We can now use the estimated phase to retrieve the original object from the diversity images using a multi-frame Wiener filter (eq. (4-11)), and the result are shown in Figure 5-5. The estimated object resembles the original one despite some blur and minor artifacts. As a measure to quantify this resemblance, we can compute the Structural Similarity Index Measure (SSIM) using the corresponding Matlab command. This metric gives a number from zero to one, where one means that the images are exactly the same. In this case, the SSIM was equal to 0.5766. Qualitatively, we can conclude that deconvolving using the estimated phase produces an image that shows much more detail compared to the one recorded at the focal point.

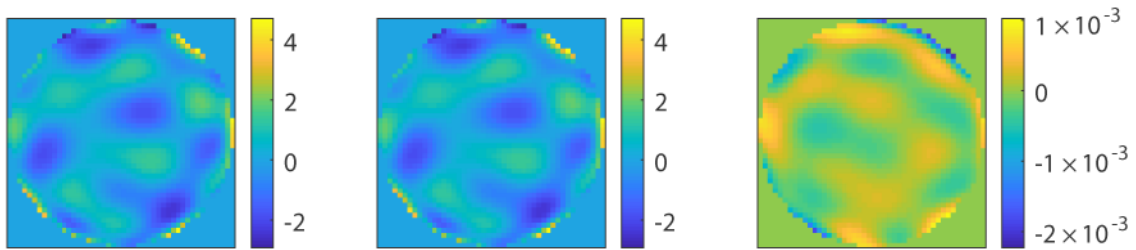


Figure 5-4: Reconstructed (left), original (middle) and residual (right) phase aberration when using Zernike basis functions and exact knowledge of the amplitude \mathcal{X} . Relative RMS error 0.0003.

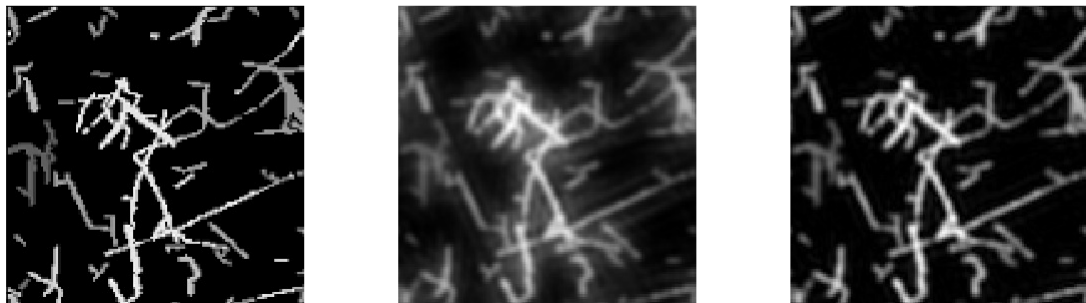


Figure 5-5: (Left) Original object. (Middle) On focus aberrated image. (Right) Result of multi-frame Wiener filter deconvolution using the images shown in Figure 5-3 and the phase retrieved in Figure 5-4. SSIM 0.5766.

5-2 Retrieval of Amplitude and Phase Aberrations

In most real world examples however, the amplitude of the pupil function will not be exactly a circle function. Often, the beam of light might be slightly dimmed at the edges of the support. In Figures 5-6, 5-7, and 5-8 we see the effect on the PSFs and the diversity images when the amplitude is Gaussian within its support. To the eye, the effect is barely noticeable compared to Figures 5-2 and 5-3.

We can now try to estimate the phase from the images seen in Figure 5-8 assuming that the amplitude is 1 inside the support and 0 outside and check how this wrong a priori informa-

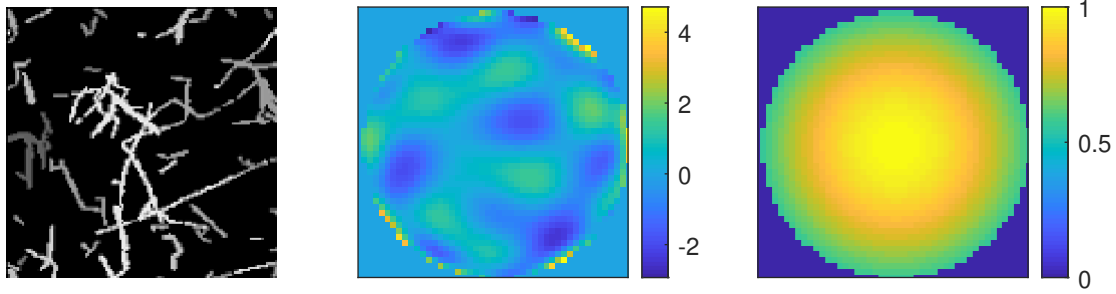


Figure 5-6: Data used to simulate diversity images with Gaussian amplitude aberration. (Left) Original object o . (Middle) Phase aberration Φ . (Right) Amplitude aberration \mathcal{X} .

$z_d = -1.5\text{e-}06\text{m}$ $z_d = -7.5\text{e-}07\text{m}$ $z_d = 0\text{m}$ $z_d = 7.5\text{e-}07\text{m}$ $z_d = 1.5\text{e-}06\text{m}$

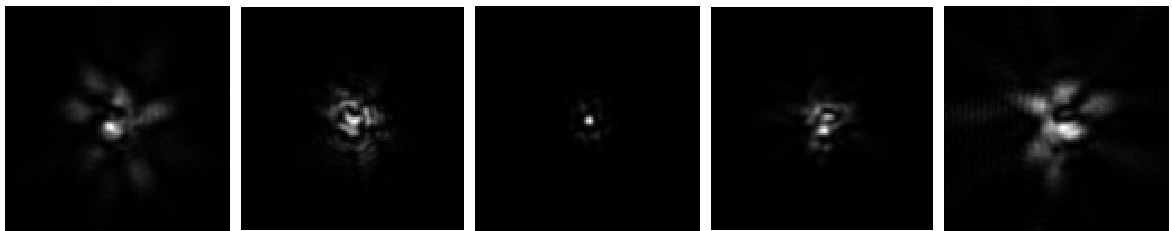


Figure 5-7: PSFs at different defocus distances using the data seen in Figure 5-6.

$z_d = -1.5\text{e-}06\text{m}$ $z_d = -7.5\text{e-}07\text{m}$ $z_d = 0\text{m}$ $z_d = 7.5\text{e-}07\text{m}$ $z_d = 1.5\text{e-}06\text{m}$

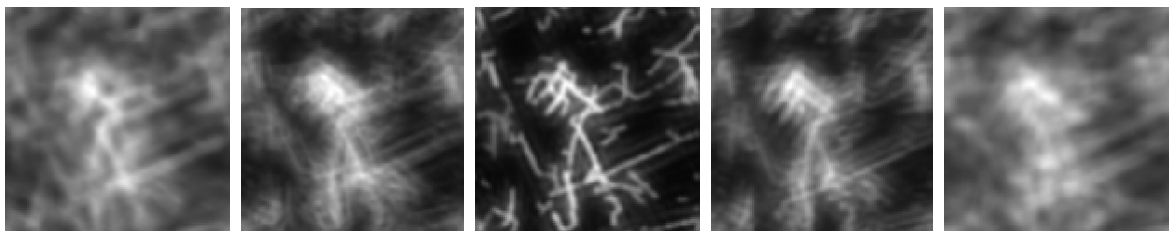


Figure 5-8: Aberrated images at different defocus distances using the data seen in Figure 5-6. SNR 50dB.

tion will effect the estimate. As before, we proceed by estimating phase only using Zernike polynomials as basis functions with radial degree from 2 to 9. In Figures 5-9 and 5-10 we see that the wrong assumption has reduced the quality of the retrieved phase and object (to a Relative RMS error of 0.4842 and SSIM 0.4722 respectively) compared to the previous estimate, where we had exact knowledge of the amplitude. In particular the phase's residual is higher at the edges of the pupil, where the wrong a priori information about the amplitude differs the most from the true Gaussian shape.

For this reason we have decided to implement in the algorithm also the possibility to estimate the amplitude of the pupil function. In principle, we could also use a set of Zernike polynomials as we did for the phase. In practice, amplitude aberrations, at least the ones arising from atmospheric scintillation [37], show more power at higher frequencies compared to phase aberrations, making Zernike based estimation less effective. This is why we decided, even in this demonstration, to retrieve the amplitude using a pixel-by-pixel approach where the

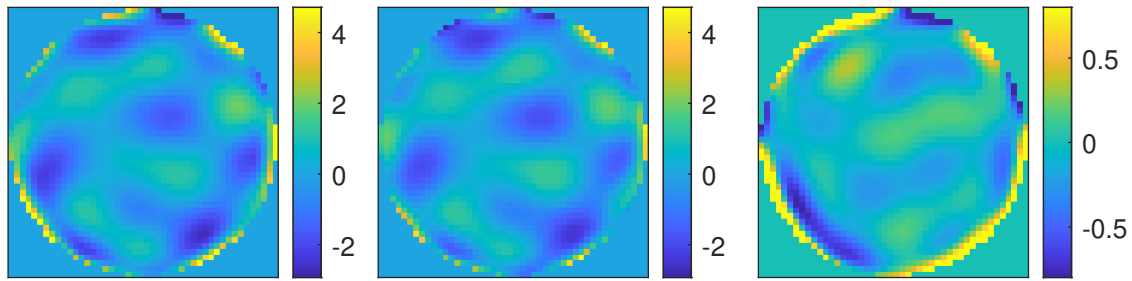


Figure 5-9: Reconstructed (left), original (middle) and residual (right) phase aberration when using Zernike basis functions and assuming the amplitude to be unitary within the support while actually it is a Gaussian (Figure 5-6). Relative RMS error 0.4842.

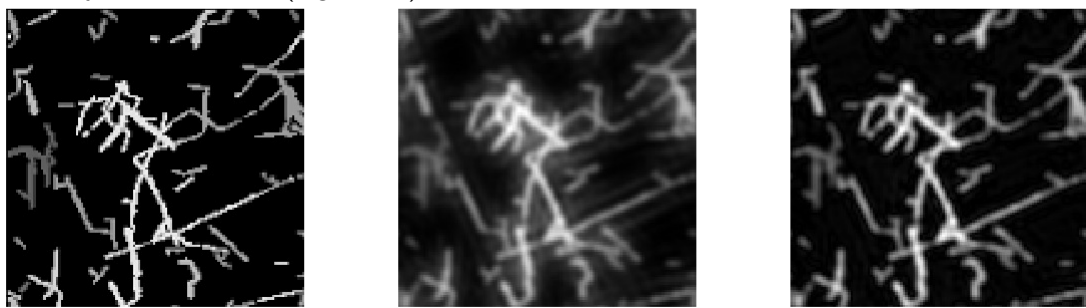


Figure 5-10: (Left) Original object. (Middle) On focus aberrated image. (Right) Result of multi-frame Wiener filter deconvolution using the images shown in Figure 5-8 and the phase retrieved in Figure 5-9. SSIM 0.4722.

gradient is given in eq. (4-26). In Figure 5-12, 5-13 and 5-14 we show the estimated phase, amplitude and object. By estimating the amplitude instead of making wrong assumptions, we have reduced the relative RMS error on the phase from 0.4842 to 0.0179 and increased the SSIM of the retrieved object from 0.4722 to 0.6038.

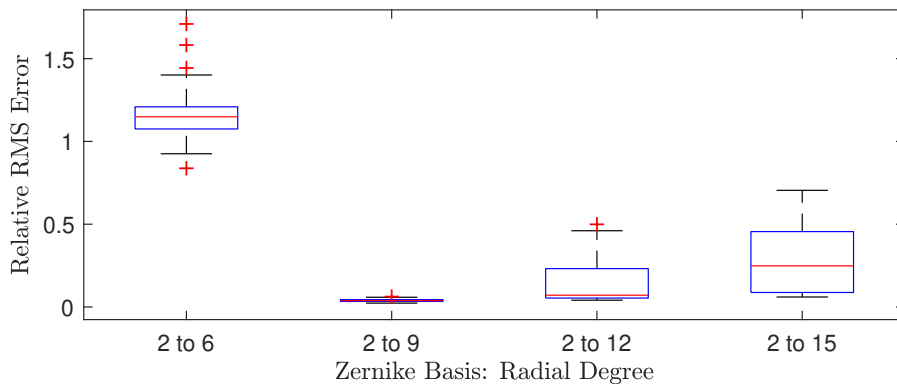


Figure 5-11: Phase only estimate using different numbers of Zernike basis. The original phase aberrations were created with Zernike polynomials with radial degree from 2 to 9 and Gaussian noise was added to the diversity images for a SNR of 15dB. The plot shows the median, the 25th and 75th percentiles, the extremes and the outliers of the relative RMS errors of the retrieved phases over 20 experiments for each box.

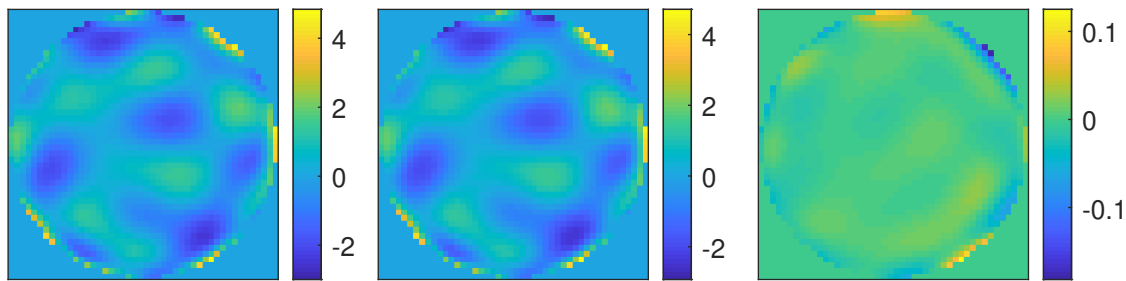


Figure 5-12: Reconstructed (left), original (middle) and residual (right) phase aberration when using Zernike basis functions for the phase and estimating the amplitude pixel-by-pixel. Relative RMS error 0.0179.

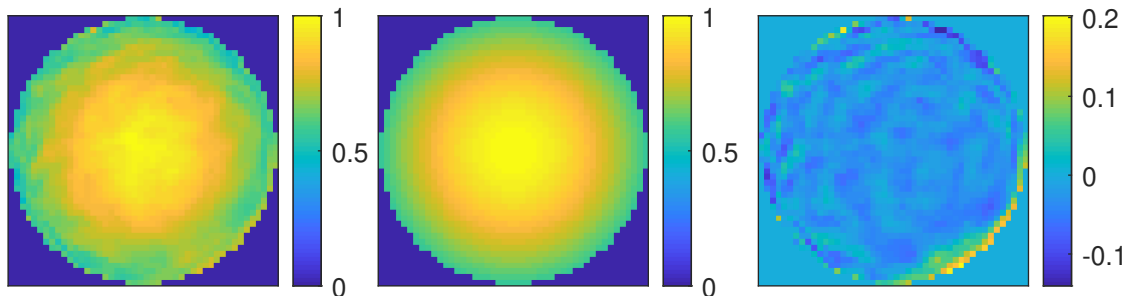


Figure 5-13: Reconstructed (left), original (middle) and residual (right) amplitude aberration using a pixel-by-pixel approach. Relative RMS error 0.0515.

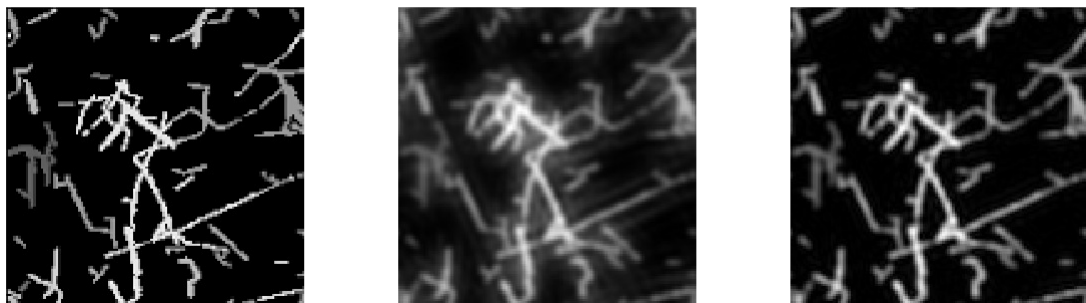


Figure 5-14: (Left) Original object. (Middle) On focus aberrated image. (Right) Result of multi-frame Wiener filter deconvolution using the images shown in Figure 5-8, the phase retrieved in Figure 5-12, and the amplitude retrieved in Figure 5-13. SSIM 0.6038.

Up to now we have always used the same Zernike polynomials both to create and retrieve the phase aberration. But what happens when we use more or less polynomials than needed? In Figure 5-11 we see that when less polynomials are used, the algorithm tries to fit the low order modes as best as possible, but the missing higher order modes still result in a very high relative RMS error. When the basis are the same as the ones used to create the aberration (radial degree from 2 to 9) we obtain an impressive suppression of the noise (the diversity images had a SNR of 15dB) with a median relative RMS error of 0.0384. When we use more modes to retrieve the aberration than the ones that were originally used to create it, we give the algorithm more degrees of freedom. In a relatively high noise setting as this one, overfitting might become an issue. As we see in Figure 5-11, this results in higher errors. Such an issue could be limited by applying, for example, L1 or L2 regularization.

5-3 Discontinuous Phase

In case no suitable basis function can be found for the application, e.g. when the phase is discontinuous, we can retrieve both the phase and the amplitude using a pixel-by-pixel approach. In Figure 5-15 we see the discontinuous phase and the Gaussian amplitude used to create the diversity images in Figure 5-17. The discontinuous phase was created by overlapping to a continuous phase the logo of Delft Center for Systems and Control (DCSC). Gaussian noise is then added to the diversity images for a SNR of 50dB.

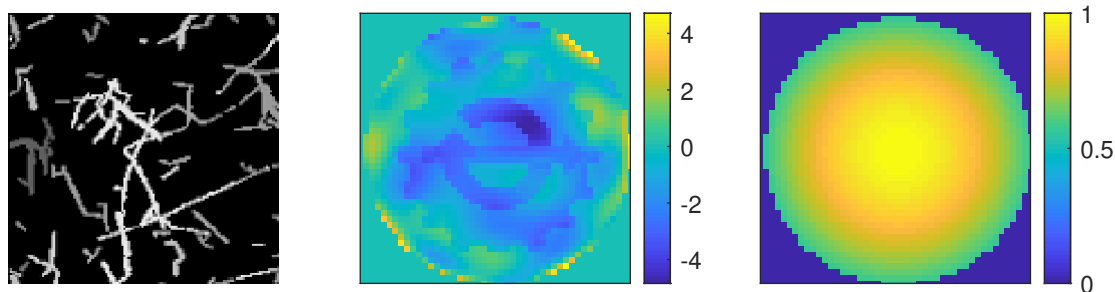


Figure 5-15: Data used to simulate diversity images with discontinuous phase aberration. (Left) Original object o . (Middle) Phase aberration Φ . (Right) Amplitude aberration \mathcal{X} .

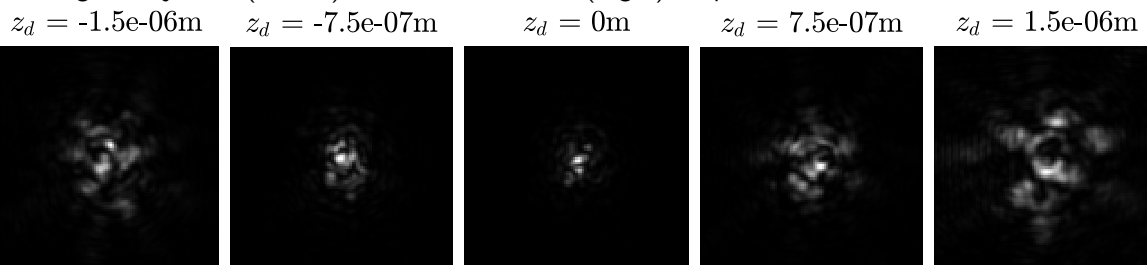


Figure 5-16: PSFs at different defocus distances using the data seen in Figure 5-15

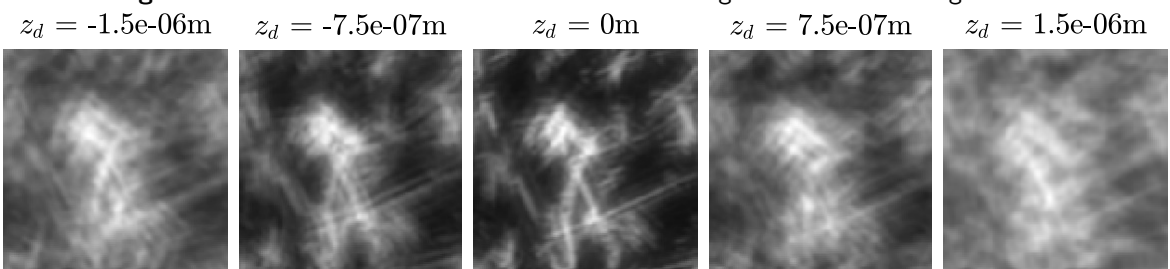


Figure 5-17: Aberrated images at different defocus distances using the data seen in Figure 5-15. SNR 50dB.

The phase and amplitude are retrieved pixelwise using the conjugate gradient method, where the explicit gradients are shown in eq. (4-22) and (4-26). The results, shown Figures 5-18, 5-19 and 5-20, present a much noisier estimate of phase and amplitude, which resulted in a higher relative RMS error and therefore a worse estimate of the original object compared to when Zernike basis were used. Nevertheless, the DCSC logo is perfectly visible in the

retrieved phase and the estimated amplitude still closely resembles the original Gaussian shape. A higher number of diversity images or better a priori knowledge of the amplitude might help reducing the noise on the retrieved functions.

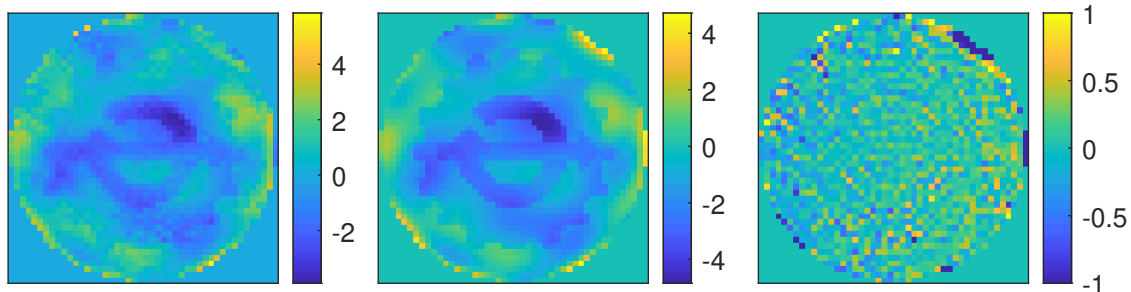


Figure 5-18: Reconstructed (left), original (middle) and residual (right) phase aberration using a pixel-by-pixel approach. Relative RMS error 0.3585.

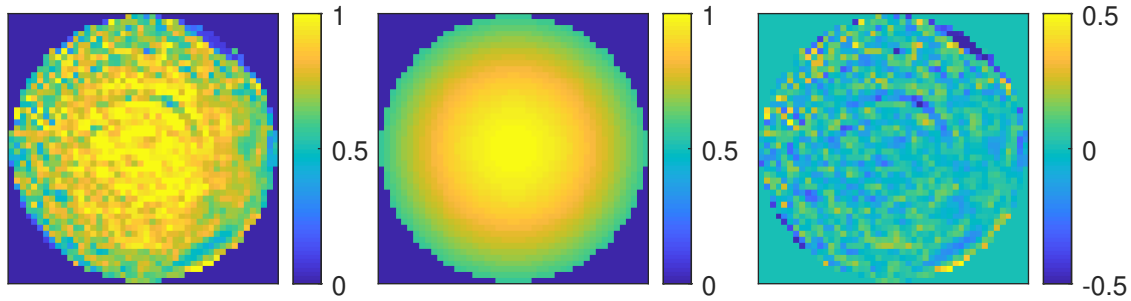


Figure 5-19: Reconstructed (left), original (middle) and residual (right) amplitude aberration using a pixel-by-pixel approach. Relative RMS error 0.1785.

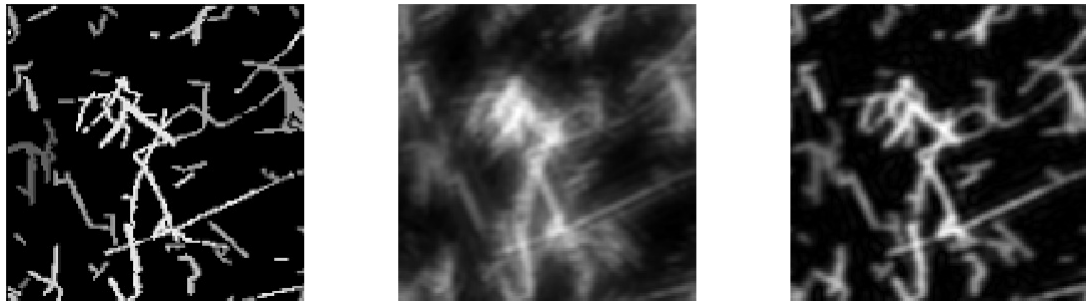


Figure 5-20: (Left) Original object. (Middle) On focus aberrated image. (Right) Result of multi-frame Wiener filter deconvolution using the images shown in Figure 5-17, the phase retrieved in Figure 5-18, and the amplitude retrieved in Figure 5-19. SSIM 0.3982.

5-4 Comparison Between Scalar and Vectorial Model

Expanding the model from scalar (eq. (2-14)) to vectorial (eq. (2-24)) indeed adds more complications, having to compute six Fourier transforms instead of one every time a PSF has to be calculated. This directly reflects on a (approximately six times) longer computation time to retrieve the phase, which can take around five minutes for five 120x120 pixels diversity

images on an average laptop computer. The question now is whether accounting for the bending of the polarization vector actually increases the accuracy of our retrieved phase.

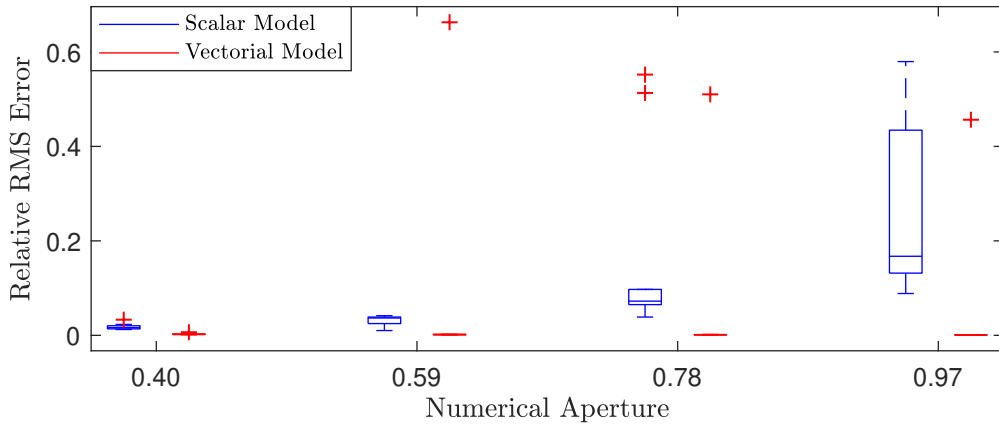


Figure 5-21: Phase only estimate using Zernike basis. With the refractive index set to one, the Numerical Aperture (NA) is increased from 0.4 to 0.97, and the phase is retrieved using both a scalar and a vectorial based algorithm. The diversity images had a SNR of 50dB. The plot shows the median, the 25th and 75th percentiles, the extremes and the outliers of the relative RMS errors of the retrieved phases over 20 experiments for each box.

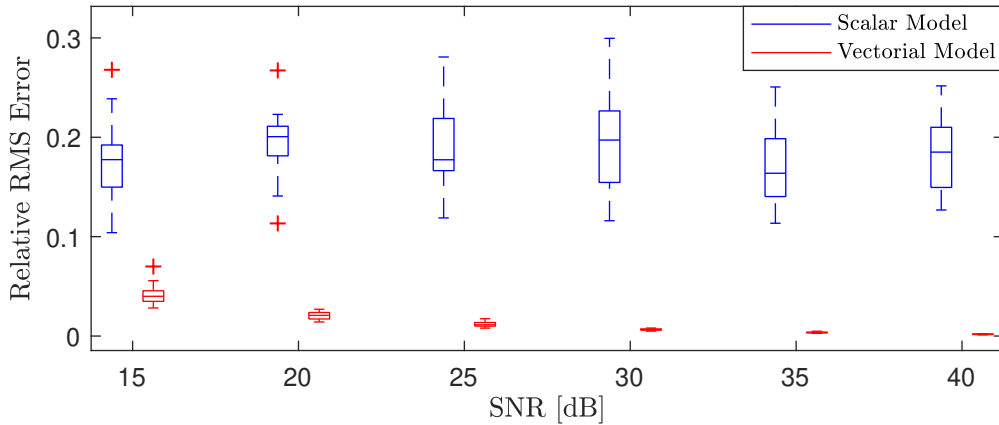


Figure 5-22: Phase only estimate using Zernike basis. With the refractive index set to 1.518 and the NA equal to 1.49, the SNR of the diversity images is increased from 15dB to 40dB, and the phase is retrieved using both a scalar and a vectorial based algorithm. The plot shows the median, the 25th and 75th percentiles, the extremes and the outliers of the relative RMS errors of the retrieved phases over 20 experiments for each box.

In Figure 5-21 we have created images with gradually increasing NA and retrieved the phase using a scalar based algorithm [15, 16] and our vectorial extension. For an NA of 0.40 the algorithms have similar performances, retrieving phases with approximately the same error. However, while the performances of vectorial based algorithm stay constant with a median relative RMS error in the order of 10^{-3} , the algorithm based on the scalar model performs worse as the NA increases. For a NA of 0.97 the scalar based algorithm has a median error

of 0.1674 with a large variance, while the vectorial algorithm is still around 0.001. Similar results were found in a recent paper about vectorial phase retrieval [9].

In Figure 5-22 we instead have kept constant the refractive index to 1.518 and the NA to 1.49, while increasing the SNR on the diversity images. In [9], they have concluded that the vectorial based algorithm is more sensitive to noise and therefore only worth using when the images have a SNR of 30dB or higher. Since our joint estimation algorithm allows us to make use of Zernike basis functions, which help us suppressing the noise and avoid overfitting, we can show that using the vectorial model can result in approximately a 6.5 times lower error even when the SNR is only 15dB.

Chapter 6

Experimental Data

Because of the great results obtained in simulation, we have decided to move forward and test our algorithm on real images obtained from a microscope in our lab. The microscope is imaging 500nm fluorescent beads recorded with 640nm light, with immersion oil with refractive index 1.518 and an objective with Numerical Aperture (NA) 1.49 and 2mm focal length. The pixel size is 81.25nm in the sample plane, making the beads approximately 6 pixels in diameter and therefore of non-negligible size.



Figure 6-1: Images of the same out-of-focus aberrated bead. (Left) Image resulted as the average of 69 images of the same bead subject to the same aberrations. (Right) Single image as recorded by the sensor.

With the idea of calibrating a Deformable Mirror (DM) with 69 actuators a large stack of images was recorded, where 40 out-of-focus images were taken at a $4/39\mu\text{m}$ distance from each other for each of the five positions of each of the 69 actuators of the mirror. Because of this, we had 69 images of the same bead subject to the same aberrations for each out-of-focus position. To improve the Signal to Noise Ratio (SNR) we have averaged all of these images. In Figure 6-1 we can see on the right a single recorded image, while on the left we see the average over 69 images. Clearly the SNR was improved by averaging, allowing us to get a clearer picture of the bead, while perhaps some blur was introduced due to misalignment between the images.

Our method for retrieval, however, is based on the assumption that the noise on the images is Gaussian. On the left of Figure 6-2 we see that the background noise of the averaged image fits a Gaussian curve. When performing a Kolmogorov-Smirnov test we accept that the noise comes from a normal distribution with p-value 0.35. When the images are not averaged and a single image is taken, we can clearly see the discrete photon count, and the distribution resembles a Poisson distribution.

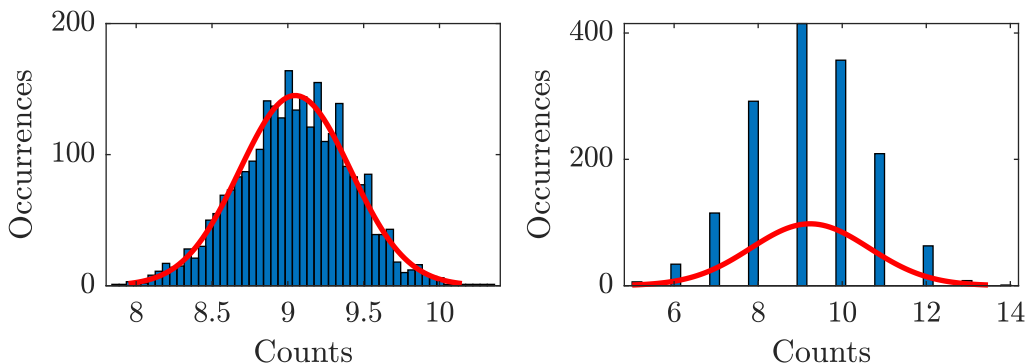


Figure 6-2: Background noise distribution of (left) the average image over 69 measurements and (right) a single image as recorded by the sensor. The Kolmogorov-Smirnov test accepts that the noise comes from a standard normal distribution with p-value 0.35 when the images are averaged (left), while it rejects the null hypothesis on the single image (right).

We therefore start by retrieving the object and complex pupil function of the averaged images. To do so, we use Zernike basis functions with radial degree from 2 to 15 to estimate the phase, while we use a pixel-by-pixel approach for the amplitude. Since it is very likely that the actual amplitude of the microscope is not a perfect circle function, we set the initial estimate for the amplitude as Gaussian to encourage convergence.

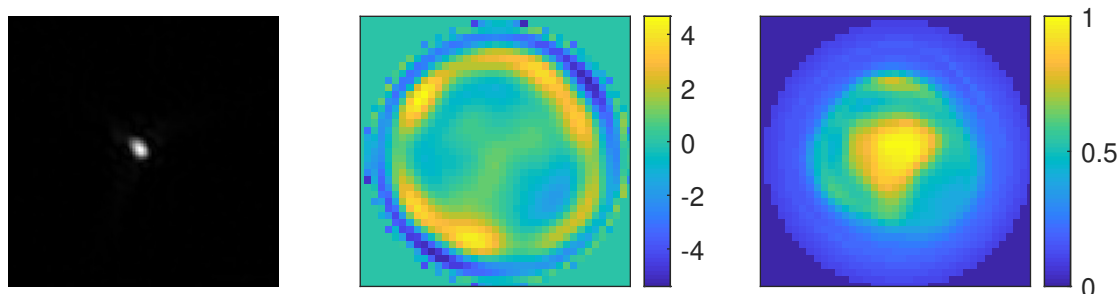


Figure 6-3: Reconstructed (left) object, (middle) phase and (right) amplitude aberrations from 40 averaged diversity images when all the DM actuators are at rest.

The reconstructed object, seen at the left of Figure 6-3, is quite close to the approximately six pixels in diameter bead that was used for the experiment. A slight blur and minor artifacts are present in the estimate of the object, but these might also be due to the averaging of several images that are slightly misaligned (see left of Figure 6-1 compared to the right). The estimated amplitude, on the right of Figure 6-3, presents large aberration, where the size of the beam is much smaller than the expected one, i.e. the amplitude is almost zero on a thick band around the edges of the pupil. Where the amplitude is almost zero, i.e. where almost

no light passes through, the phase does not influence the diversity images that much. For this reason we can rely on the phase estimate (middle of Figure 6-3) only in the central part of the pupil.

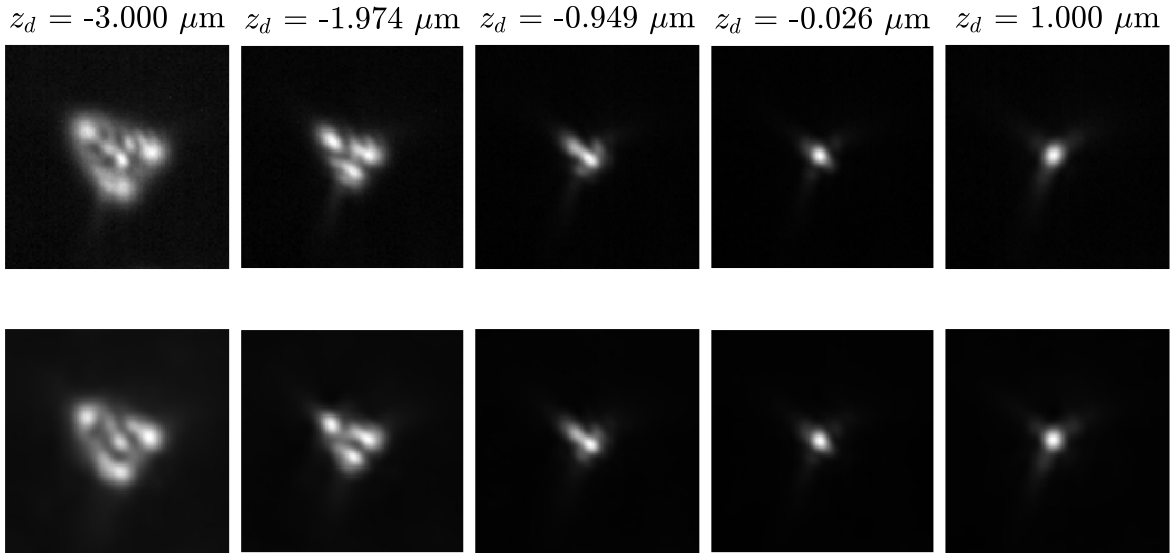


Figure 6-4: (Top) Five of the 40 original out-of-focus diversity images used for retrieval. (Bottom) Five of the reconstructed diversity images using the estimated data and the vectorial model. The reconstructed and original images agree with a mean Structural Similarity Index Measure (SSIM) of 0.9618.

In Figure 6-4 we can see, at the top, five of the original 40 images we have used for the retrieval. At the bottom, we have used the estimated object and pupil function shown in Figure 6-3 to recreate the original images. The original and reconstructed diversity images agree with a mean SSIM of 0.9618. We can now try to run the algorithm with the same settings on the non-averaged images with predominantly Poisson noise to check robustness of the algorithm to higher levels of noise and a different distribution.

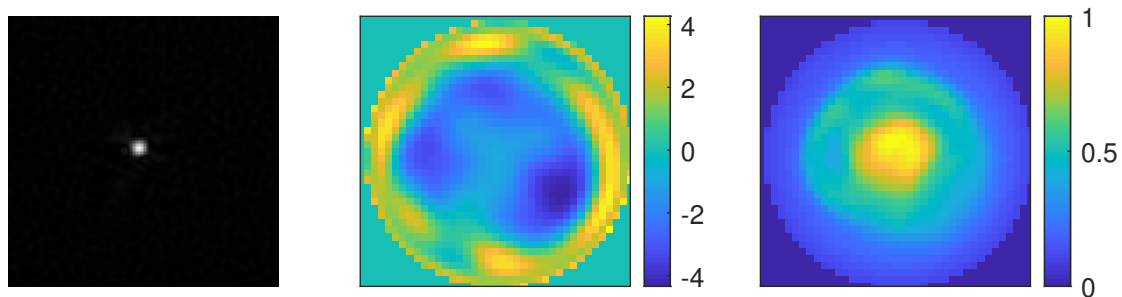


Figure 6-5: Reconstructed (left) object, (middle) phase and (right) amplitude aberrations from 40 diversity images when all the DM actuators are at rest.

In Figure 6-5 we see that the estimated object is almost exactly a 6 pixels in diameter bead and, compared to the retrieved object in Figure 6-3, we got rid of the blur. This confirms that averaging several images to increase the SNR might introduce blur due to misalignment. The estimated phase and amplitude aberrations are comparable to the previous estimate.

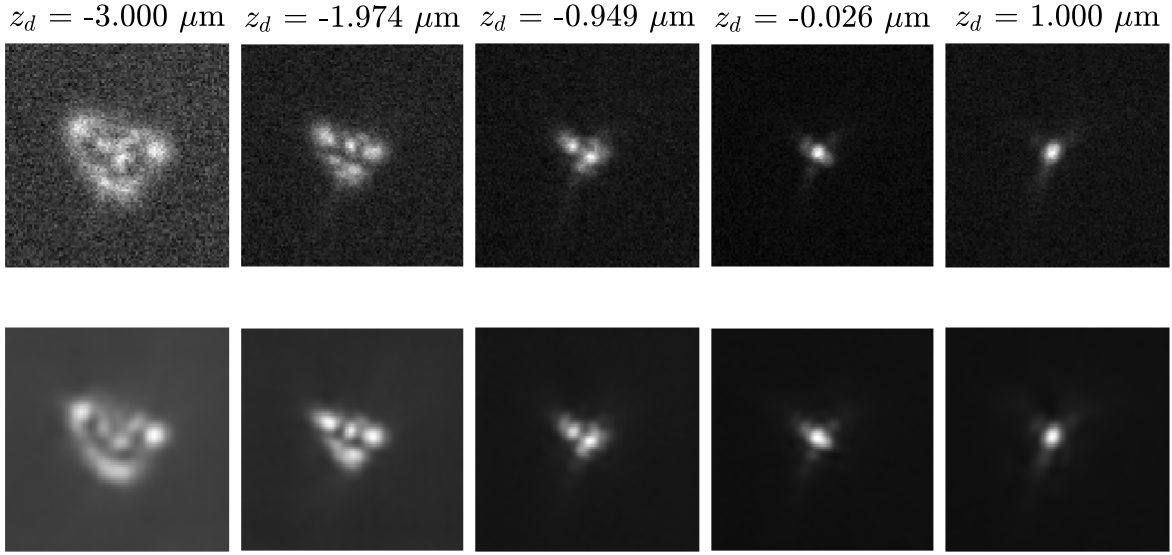


Figure 6-6: (Top) Five of the 40 original out-of-focus diversity images used for retrieval. (Bottom) Five of the reconstructed diversity images using the estimated data and the vectorial model. The reconstructed and original images agree with a mean SSIM of 0.6026.

In Figure 6-6, we see that the estimated and original diversity images agree with a SSIM of 0.6026. Visually, they look fairly close, and the relatively low value of SSIM might be attributed to the high level of noise in the original images. Overall, the algorithm seems to be able to produce satisfying results even with low SNR Poisson noise and large amplitude aberrations.

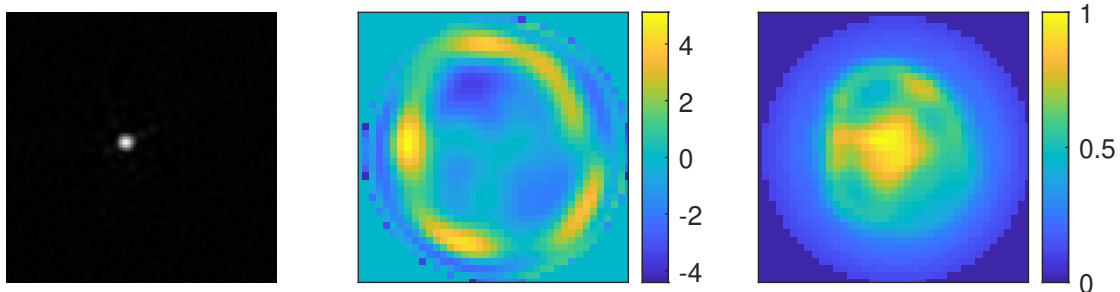


Figure 6-7: Reconstructed (left) object, (middle) phase and (right) amplitude aberrations from 40 diversity images when actuator 31 comes one step forward.

We can now try to actuate the DM and see if we are able to retrieve the influence function of an actuator. In Figures 6-7 and 6-8 we see the retrieved object, phase and amplitude when actuator 31 comes one and two steps forward respectively. From how the amplitude aberration evolves, we can observe that while the actuator comes forward, the beam is deformed and squeezed from the left. The phase seems also to be pushed forward in the middle-left of the pupil.

If we now have the retrieved phase aberrations when the actuator is at rest, one step or two steps forward, we can extract the influence function by subtracting the phase retrieved when

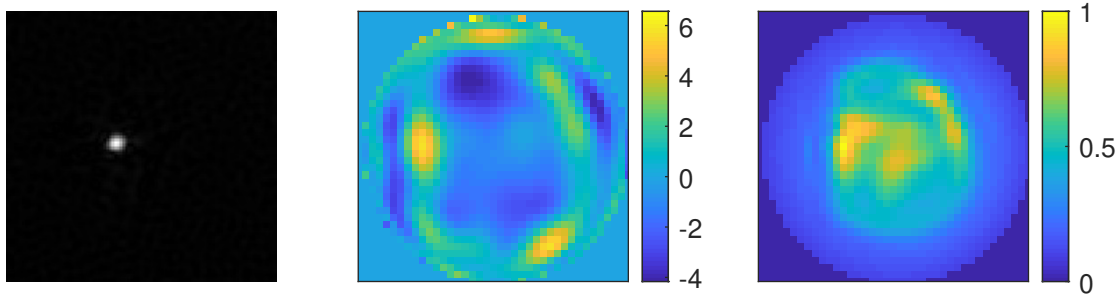


Figure 6-8: Reconstructed (left) object, (middle) phase and (right) amplitude aberrations from 40 diversity images when actuator 31 comes two steps forward.

the mirror is at rest from the phase retrieved when the mirror is actuated. In Figure 6-9, we observe that at the middle-left of the pupil the phase is pushed up by the actuator, with increasing magnitude when a higher voltage is applied.

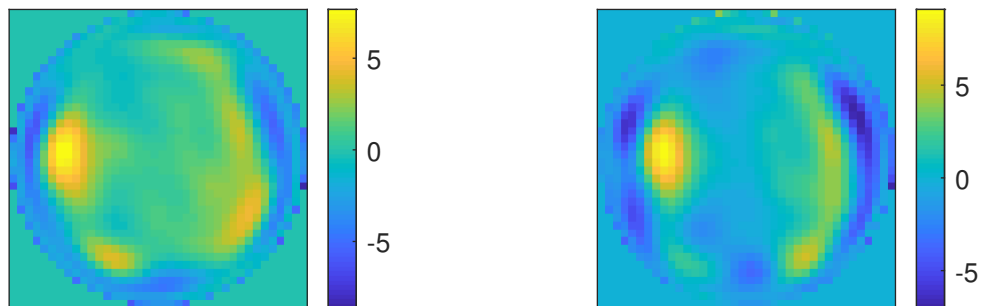


Figure 6-9: (Left) Phase retrieved when the DM's actuator number 31 is one step forward (Figure 6-7) minus the reference phase (Figure 6-5). (Right) Phase retrieved when the DM's actuator number 31 is two steps forward (Figure 6-8) minus the reference phase (Figure 6-5).

However, the quality of the estimated influence function is still very low since, due to the almost zero amplitude at the edges of the pupil, the phase estimates at the border are unreliable. Therefore, the results are still quite inconclusive, and higher quality images are needed.

Chapter 7

Conclusions and Future Work

In this thesis we have rigorously derived vectorial Point Spread Function (PSF) model that has sometimes been used in literature with little explanation. We have modified an existing joint estimation method to use this vectorial model and computed explicit derivatives with respect to phase and amplitude parameters. Through simulation we have shown that the algorithm can accurately retrieve object and complex pupil function from a set of out-of-focus images and we have demonstrated how, when imaging through a high-NA objective, the scalar model produces low quality estimates due to high model deviations. Using experimental data, we have also tested the robustness of the algorithm by showing that we are able to accurately reproduce the recorded diversity images even with highly aberrated misaligned optics and low Signal to Noise Ratio (SNR) images affected by Poisson noise.

The retrieved influence function from the experimental data, however, was still not satisfying in quality. Some misalignment in the optics probably reduced the overall numerical aperture of the system, preventing us from properly estimating the phase over the whole pupil. Also because of the lower numerical aperture and, in addition, the high level of noise, we couldn't show the increased quality of the estimates using the vectorial model compared to the scalar one from the experimental data.

This all calls for images from a better quality setup, where proper conclusion regarding the superiority of the vectorial model in high-NA systems can be drawn. To further confirm this, the estimated phase should be compared to the one detected by some wavefront sensing hardware, e.g. a Shack–Hartmann sensor. Also, with a properly calibrated Deformable Mirror (DM), we could introduce, estimate, and compensate phase aberrations using our phase estimation scheme, thus providing more evidence to confirm the quality of the estimates.

When using Zernike basis, simple L1 or L2 regularization could be introduced to encourage the use of the lower-order modes over the higher-order ones, thus limiting the increased error seen in Figure 5-11 when too many Zernike polynomials are used. Also, the algorithm was implemented in Matlab to test its performances, but little care was put into making the algorithm computationally efficient. By rewriting the code into a different language with an eye to the number of computations, the total time for retrieving the data could be reduced dramatically.

The algorithm hasn't been tested on thick samples, where different layers of the specimen are subject to slightly different defociuses. In a recent paper [38], phase diversity was used to estimate phase aberrations in three-dimensional samples using a technique that closely relates to ours. A vectorial model could be easily introduced in their scheme. A different problem formulation was instead proposed in [39], where the cost function was enforcing spatial uncorrelation of the residual diversity images. A comparison between the performances of our and their approach would be of interest.

To conclude, what we have understood from this research is that joint estimation is a powerful and versatile tool that can be easily modified and tailored to the application. Our expansion to a vectorial model promises great improvements in the estimates of object and pupil function in high-NA settings, and for this reason the author suggests further experimentation in this direction.

Appendix A

Appendix: Scalar Diffraction Theory

A-1 Light as an Electromagnetic Radiation

According to the wave theory of light, light is electromagnetic radiation that, as such, satisfies Maxwell's equations. In absence of free charge, such equations are given by:

$$\begin{aligned}\nabla \times \vec{\mathcal{E}} &= -\mu \frac{\partial \vec{\mathcal{H}}}{\partial t} \\ \nabla \times \vec{\mathcal{H}} &= \epsilon \frac{\partial \vec{\mathcal{E}}}{\partial t} \\ \nabla \cdot \epsilon \vec{\mathcal{E}} &= 0 \\ \nabla \cdot \mu \vec{\mathcal{H}} &= 0\end{aligned}\tag{A-1}$$

where $\vec{\mathcal{E}}$ is the electric field, $\vec{\mathcal{H}}$ is the magnetic field, and μ and ϵ are, respectively, the permeability and the permittivity of the medium. The operators $\nabla \cdot$ and $\nabla \times$ represent, respectively, the divergence and the curl operator. If the propagation of the wave is linear, isotropic, homogeneous, and non-dispersive, we can derive the following wave equations:

$$\nabla^2 \vec{\mathcal{E}} - \frac{n^2}{c^2} \frac{\partial^2 \vec{\mathcal{E}}}{\partial t^2} = 0, \quad \nabla^2 \vec{\mathcal{H}} - \frac{n^2}{c^2} \frac{\partial^2 \vec{\mathcal{H}}}{\partial t^2} = 0\tag{A-2}$$

where $n = \sqrt{\epsilon/\epsilon_0}$ is the refractive index and $c = 1/\sqrt{\mu_0 \epsilon_0}$ is the speed of light in vacuum. As we can see, $\vec{\mathcal{E}}$ and $\vec{\mathcal{H}}$ obey the same wave equation, and thus such an equation is obeyed by each component of those vector fields, for example:

$$\nabla^2 \mathcal{E}_x - \frac{n^2}{c^2} \frac{\partial^2 \mathcal{E}_x}{\partial t^2} = 0\tag{A-3}$$

A-1-1 The Scalar Wave

According to what we just argued, it is possible to summarize the whole vectorial electric field \vec{E} with a scalar wave $u(P, t)$ obeying the following:

$$\nabla^2 u(P, t) - \frac{n^2}{c^2} \frac{\partial^2 u(P, t)}{\partial t^2} = 0 \quad (\text{A-4})$$

This scalar equation correctly describes the magnitude of the electric field but omits information regarding the polarization of such field. If we, however, persevere with this description and pose our attention to monochromatic waves, the scalar field in a point P at time t can be expressed as:

$$u(P, t) = A(P) \cos[2\pi\nu t + \phi(P)] \quad (\text{A-5})$$

where $A(P)$ is the amplitude at point P , ν is the optical frequency, and $\phi(P)$ is the phase at point P . If we use complex notation:

$$\begin{aligned} u(P, t) &= \Re\{U(P)e^{-2\pi i \nu t}\} \\ U(P) &= A(P)e^{-i\phi(P)} \end{aligned} \quad (\text{A-6})$$

The photodetector of a camera usually generates a photocurrent linearly proportional to the incident power of the electric field. If we assume that the wave is propagating in a direction nearly normal to the one of the detector, this incident power over a surface A is simply the integral of the power density over such area. We can express the intensity of a scalar monochromatic wave at point P as the squared magnitude of the complex phasor representation $U(P)$ of the disturbance, that is:

$$I(P) = |U(P)|^2 \quad (\text{A-7})$$

We note that the measured power density and the intensity of the scalar field are not identical, but are however directly proportional. For this reason, we will refer to the intensity as our sensor's measurement.

A-2 Wave propagation

Now that we have a way to describe light as a scalar field and we know how it is recorded by a sensor, we want to understand how it propagates through a medium.

A-2-1 Huygens-Fresnel Principle

We will now just briefly demonstrate the Huygens-Fresnel principle using the example shown in Figure A-1. Given a scalar field distribution U on a plane (ξ, η) and a finite aperture Σ , what is the field distribution on a parallel plane (x, y) ?

The Huygens-Fresnel principle tells us that such a field distribution at a point P_0 on the plane (x, y) is given by:

$$U(P_0) = \frac{z}{i\lambda} \iint_{\Sigma} U(\xi, \eta) \frac{e^{ikr_{01}}}{r_{01}^2} d\xi d\eta, \quad r_{01} = \sqrt{z^2 + x^2 + y^2} \quad (\text{A-8})$$

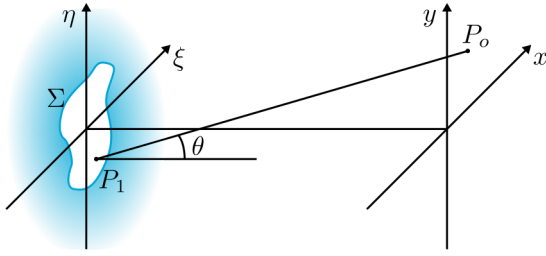


Figure A-1: Wave propagation through an aperture Σ .

where $k = 2\pi/\lambda$ is the wave number and $\lambda = v/\nu$ is the wavelength, where v is the wave propagation velocity through the medium. This equation stems from the fact that, according to Huygens, each point on a wavefront is the source of a spherical wavelet, and these secondary wavelets mutually interfere.

A-2-2 Fresnel Diffraction

To reduce complexity of the integral in eq. (A-8), Fresnel introduces binomial expansion ($\sqrt{1+b} = 1 + 1/2b + 1/8b^2 + \dots$) to the expression of r_{01} , that is:

$$\begin{aligned} r_{01} &= z \sqrt{1 + \left(\frac{x-\xi}{z}\right)^2 + \left(\frac{y-\eta}{z}\right)^2} \\ &\approx z \left[1 + \frac{1}{2} \left(\frac{x-\xi}{z} \right)^2 + \frac{1}{2} \left(\frac{y-\eta}{z} \right)^2 \right] \approx z \end{aligned} \quad (\text{A-9})$$

How do we decide whether to keep the zero or first order approximation? The r_{01} that appears in the denominator in eq. (A-8) can be just approximated with z . At the exponent, since r_{01} is multiplied by a large number k and a small change in phase leads to non-negligible changes in the integral, we keep the whole quadratic term. The latter approximation substitutes the sphere $r_{01}^2 = x^2 + y^2 + z^2$ (spherical wavefront) with an ellipsoid $r_{01} = z + \frac{x^2}{2z} + \frac{y^2}{2z}$ (parabolic wavefront), and it also known as paraxial approximation.

$$\begin{aligned} U(x, y) &= \frac{z}{i\lambda} \iint_{-\infty}^{\infty} U(\xi, \eta) e^{ik\left(z+\frac{1}{2}\frac{(x-\xi)^2}{z}+\frac{1}{2}\frac{(y-\eta)^2}{z}\right)} \frac{1}{z^2} d\xi d\eta \\ &= \frac{e^{ikz}}{i\lambda z} \iint_{-\infty}^{\infty} U(\xi, \eta) e^{\frac{ik}{2z}((x-\xi)^2+(y-\eta)^2)} d\xi d\eta \end{aligned} \quad (\text{A-10})$$

This equation can be seen as a convolution against the kernel h , thus obtaining:

$$U(x, y) = \iint_{-\infty}^{\infty} U(\xi, \eta) h(x - \xi, y - \eta) d\xi d\eta, \quad h(x - \xi, y - \eta) = \frac{e^{ikz}}{i\lambda z} e^{\frac{ik}{2z}} \quad (\text{A-11})$$

Or as, up to constant terms, a Fourier Transform of the aperture field and a quadratic phase exponential:

$$U(x, y) = \frac{e^{ikz}}{i\lambda z} e^{\frac{ikz}{2z}(x^2+y^2)} \iint_{-\infty}^{\infty} \left\{ U(\xi, \eta) e^{\frac{ikz}{2z}(\xi^2+\eta^2)} \right\} e^{-\frac{2\pi i}{\lambda z}(x\xi+y\eta)} d\xi d\eta \quad (\text{A-12})$$

A-2-3 Fraunhofer Diffraction

Fraunhofer further simplifies eq. (A-12) by getting rid of the quadratic phase exponential as follows:

$$e^{i\frac{1}{z}\frac{k}{2}(\xi^2+\eta^2)} \approx e^0 = 1 \quad (\text{A-13})$$

This approximation is sometimes known as far field, as it is valid only if $z \gg k(\xi^2 + \eta^2)_{\max}/2$, meaning that the field is observed at a distance that is a much greater than the maximum size of the aperture. The simplified diffraction integral becomes:

$$\begin{aligned} U(x, y) &= \frac{e^{ikz}}{i\lambda z} e^{\frac{ikz}{2z}(x^2+y^2)} \iint_{-\infty}^{\infty} U(\xi, \eta) e^{2\pi i(\frac{x\xi}{\lambda z} + \frac{y\eta}{\lambda z})} d\xi d\eta \\ &= \frac{e^{ikz}}{i\lambda z} e^{\frac{ikz}{2z}(x^2+y^2)} \mathcal{F}U\left(\frac{x}{\lambda z}, \frac{y}{\lambda z}\right) \end{aligned} \quad (\text{A-14})$$

where with \mathcal{F} we represent the Fourier Transform.

Appendix B

Appendix: Vectorial Diffraction Theory

B-1 Ray Tracing in Microscope Objectives

Let us first derive the multiplication of the Jones matrices shown in eq. (2-21) by simply using the table found in [22], that is:

$$\mathbb{R}_z^{-1}(\phi)\mathbb{L}(-\theta)\mathbb{R}_z(\phi) = \begin{bmatrix} \cos^2 \phi \cos \theta + \sin^2 \phi, & \cos \phi \sin \phi \cos \theta - \sin \phi \cos \phi, & -\cos \phi \sin \theta \\ \cos \phi \sin \phi \cos \theta - \sin \phi \cos \phi, & \sin^2 \phi \cos \theta + \cos^2 \phi, & -\sin \phi \sin \theta \\ \cos \phi \sin \theta, & \sin \phi \sin \theta, & \cos \theta \end{bmatrix} \quad (\text{B-1})$$

We can now compute the field behind the lens produced by the x component of the dipole by simple multiplication of the matrix above and the field \vec{E}_x as given in eq. (2-18) (the multiplicative term p_x is neglected for brevity), thus obtaining:

$$\begin{aligned} \vec{E}'_x &= \mathbb{R}_z^{-1}(\phi)\mathbb{L}(-\theta)\mathbb{R}_z(\phi)\vec{E}_x \\ &= \begin{bmatrix} \cos^3 \theta \cos^2 \phi + \cos^2 \theta \sin^2 \phi + \sin^4 \phi \sin^2 \theta + \cos^2 \phi \sin^2 \phi \sin^2 \theta + \cos^2 \phi \sin^2 \theta \cos \theta \\ \cos^3 \theta \cos \phi \sin \phi - \cos^2 \theta \sin \phi \cos \phi - \sin^3 \phi \sin^2 \theta \cos \phi - \cos^3 \phi \sin^2 \theta \sin \phi + \sin^2 \theta \sin \phi \cos \phi \cos \theta \\ 0 \end{bmatrix} \end{aligned} \quad (\text{B-2})$$

Let us now simplify the first two components (E_{xx} , E_{xy}) by making use of the Pythagorean identity ($\sin^2 \alpha + \cos^2 \alpha = 1$) obtaining:

$$\begin{aligned} E_{xx} &= (1 - \sin^2 \theta) \cos \theta \cos^2 \phi + \cos^2 \theta \sin^2 \phi + (1 - \cos^2 \phi) \sin^2 \phi \sin^2 \theta \\ &\quad + \cos^2 \phi \sin^2 \phi \sin^2 \theta + \cos^2 \phi \sin^2 \theta \cos \theta \\ &= \sin^2 \phi (\cos^2 \theta + \sin^2 \theta) + \cos^2 \phi \cos \theta \\ &= \sin^2 \phi + \cos^2 \phi \cos \theta \end{aligned} \quad (\text{B-3})$$

$$\begin{aligned} E_{xy} &= (1 - \sin^2 \theta) \cos \theta \cos \phi \sin \phi - \cos^2 \theta \sin \phi \cos \phi - (1 - \cos^2 \phi) \sin \phi \sin^2 \theta \cos \phi \\ &\quad - \cos^3 \phi \sin^2 \theta \sin \phi + \sin^2 \theta \sin \phi \cos \phi \cos \theta \\ &= \cos \theta \cos \phi \sin \phi - \cos \phi \sin \phi \end{aligned}$$

We can now do the same procedure for the other two fields, that is:

$$\vec{E}'_y = \begin{bmatrix} -\sin^3 \phi \sin^2 \theta \cos \phi - \cos^3 \phi \sin^2 \theta \sin \phi + \cos^3 \theta \cos \phi \sin \phi - \cos^2 \theta \cos \phi \sin \phi + \sin^2 \theta \sin \phi \cos \theta \cos \phi \\ \cos^2 \phi \sin^2 \phi \sin^2 \theta + \cos^4 \phi \sin^2 \theta + \cos^3 \theta \sin^2 \phi + \cos^2 \phi \cos^2 \theta + \sin^2 \phi \sin^2 \theta \cos \theta \\ 0 \end{bmatrix} \quad (\text{B-4})$$

$$\vec{E}'_z = \begin{bmatrix} -\cos^3 \phi \cos^2 \theta \sin \theta - \sin^2 \phi \cos^2 \theta \sin \theta \cos \phi - \sin^3 \theta \cos \phi \\ -\cos^2 \phi \cos^2 \theta \sin \phi \sin \theta - \sin^3 \phi \cos^2 \theta \sin \theta - \sin^3 \theta \sin \phi \\ -\cos^2 \phi \sin^2 \theta \cos \theta - \sin^2 \phi \sin^2 \theta \cos \theta + \sin^2 \theta \cos \theta \end{bmatrix} \quad (\text{B-5})$$

And their components can be simplified as:

$$\begin{aligned} E_{yx} &= -(1 - \cos^2 \phi) \sin \phi \sin^2 \theta \cos \phi - \cos^3 \phi \sin^2 \theta \sin \phi + (1 - \sin^2 \theta) \cos \theta \cos \phi \sin \phi \\ &\quad - \cos^2 \theta \cos \phi \sin \phi + \sin^2 \theta \sin \phi \cos \theta \cos \phi \\ &= \cos \theta \cos \phi \sin \phi - \cos \phi \sin \phi \end{aligned} \quad (\text{B-6})$$

$$\begin{aligned} E_{yy} &= \cos^2 \phi \sin^2 \phi \sin^2 \theta + (1 - \sin^2 \phi) \cos^2 \phi \sin^2 \theta + (1 - \sin^2 \theta) \cos \theta \sin^2 \phi \\ &\quad + (1 - \sin^2 \theta) \cos^2 \phi + \sin^2 \phi \sin^2 \theta \cos \theta \\ &= \sin^2 \phi \cos \theta + \cos^2 \phi \end{aligned}$$

$$\begin{aligned} E_{zx} &= -(1 - \sin^2 \phi) \cos \phi \cos^2 \theta \sin \theta - \sin^2 \phi \cos^2 \theta \sin \theta \cos \phi - (1 - \cos^2 \theta) \sin \theta \cos \phi \\ &= -\sin \theta \cos \phi \end{aligned}$$

$$\begin{aligned} E_{zy} &= -\cos^2 \phi \cos^2 \theta \sin \phi \sin \theta - (1 - \cos^2 \phi) \sin \phi \cos^2 \theta \sin \theta - (1 - \cos^2 \theta) \sin \theta \sin \phi \\ &= -\sin \theta \sin \phi \end{aligned} \quad (\text{B-7})$$

$$E_{zz} = -(1 - \sin^2 \phi) \sin^2 \theta \cos \theta - \sin^2 \phi \sin^2 \theta \cos \theta + \sin^2 \theta \cos \theta = 0$$

Our final goal is to express the six scalar components we just found as function of the unit vector \hat{k} as given in eq. (2-19), thus we simplify as follows:

$$\begin{aligned} E_{xx} &= \frac{(1 + \cos \theta)(\cos^2 \phi \cos \theta + \sin^2 \phi)}{1 + \cos \theta} = \frac{\cos \theta + \sin^2 \phi + \cos^2 \phi \cos^2 \theta}{1 + \cos \theta} \\ &= \frac{1 + \cos \theta - 1 + \sin^2 \phi + \cos^2 \phi \cos^2 \theta}{1 + \cos \theta} = 1 + \frac{\cos^2 \phi(\cos^2 \theta - 1)}{1 + \cos \theta} \\ &= 1 - \frac{\cos^2 \phi \sin^2 \theta}{1 + \cos \theta} = 1 - \frac{k_x^2}{1 - k_z} \\ E_{xy} = E_{yx} &= \frac{(1 + \cos \theta)(\cos \phi \sin \phi \cos \theta - \sin \phi \cos \phi)}{1 + \cos \theta} \\ &= \frac{\cos \phi \sin \phi \cos^2 \theta - \sin \theta \cos \phi}{1 + \cos \theta} = -\frac{\cos \phi \sin \phi \sin^2 \theta}{1 + \cos \theta} = -\frac{k_x k_y}{1 + k_z} \quad (\text{B-8}) \\ E_{yy} &= \frac{(1 + \cos \theta)(\sin^2 \phi \cos \theta + \cos^2 \phi)}{1 + \cos \theta} = \frac{\cos \theta + \cos^2 \phi + \sin^2 \phi \cos^2 \theta}{1 + \cos \theta} \\ &= \frac{1 + \cos \theta - 1 + \cos^2 \phi + \sin^2 \phi \cos^2 \theta}{1 + \cos \theta} = 1 + \frac{\sin^2 \phi(\cos^2 \theta - 1)}{1 + \cos \theta} \\ &= 1 - \frac{\sin^2 \phi \sin^2 \theta}{1 + \cos \theta} = 1 - \frac{k_y^2}{1 - k_z} \\ E_{zx} &= -k_x \\ E_{zy} &= -k_y \end{aligned}$$

Appendix C

Explicit Gradient

The derivative of the co-log-likelihood function with respect to a parameter α_n is given by:

$$\frac{\partial}{\partial \alpha_n} L_M = \sum_{u \in \mathcal{U}} \sum_{d=1}^m Z_d \frac{\partial}{\partial \alpha_n} H_d + c.c. \quad (\text{C-1})$$

where *c.c* stands for complex conjugate and

$$Z_d = \begin{cases} \frac{\sum_l |H_l|^2 (\sum_k R_k H_k^*) R_d^* - |\sum_k D_k H_k^*|^2 H_d^*}{(\sum_l |H_l|^2)^2} & u \in \mathcal{U}_1 \\ 0 & u \in \mathcal{U}_0 \end{cases} \quad (\text{C-2})$$

We therefore first need to find the derivative of the Optical Transfer Function (OTF). Let us remember that the vectorial intensity Point Spread Function (PSF) of diversity d is given by:

$$h_{I,d}(x) = \sum_{cc} |\mathcal{F}(E_{cc}(u) P_d(u))|^2 \quad (\text{C-3})$$

where the pupil function of diversity d is expressed as:

$$P_d(u) = \mathcal{X}(u) e^{i \left(\sum_{j=1}^J \alpha_j \Phi_j(u) + \phi_d(u) \right)} \quad (\text{C-4})$$

The OTF is then expressed as:

$$\begin{aligned} H_d(u) &= \mathcal{F} \left(\sum_{cc} |\mathcal{F}(E_{cc}(u) P_d(u))|^2 \right) \\ &= \sum_{cc} \mathcal{F} \left(|\mathcal{F}(E_{cc}(u) P_d(u))|^2 \right) \end{aligned} \quad (\text{C-5})$$

The autocorrelation theorem tells us that:

$$\mathcal{F}(|g(x)|^2) = \iint_{-\infty}^{\infty} G(u') G^*(u' - u) du' du, \quad G(u) = \mathcal{F}g(u) \quad (\text{C-6})$$

where with the asterisk * we represent the complex conjugate. In our case $g(x)$ is equal to $\mathcal{F}(E_{cc}(u)P_d(u))$, which when Fourier transformed becomes:

$$\mathcal{F}(\mathcal{F}(E_{cc}(u)P_d(u))) = E_{cc}(-u)P_d(-u) \quad (\text{C-7})$$

We now have a way to rewrite our OTF. Given that all the signals are actually sampled (we have pixels instead of a continuous functions) we will use a discrete version of the autocorrelation theorem.

$$\begin{aligned} H_d(u) &= \frac{1}{N^2} \sum_{cc} \sum_{u' \in \mathcal{U}} E_{cc}(-u') P_d(-u') E_{cc}(u - u') P_d^*(u - u') \\ &= \frac{1}{N^2} \sum_{cc} \sum_{u'' \in \mathcal{U}} E_{cc}(u'') P_d(u'') E_{cc}(u + u'') P_d^*(u + u'') \end{aligned} \quad (\text{C-8})$$

where we have performed a change of variables $u'' = -u'$. Let us now compute the derivatives of such OTF as:

$$\begin{aligned} \frac{\partial}{\partial \alpha_n} H_d(u) &= \frac{1}{N^2} \sum_{cc} \sum_{u'' \in \mathcal{U}} E_{cc}(u'') E_{cc}(u + u'') \left(\frac{\partial}{\partial \alpha_n} P_d(u'') P_d^*(u + u'') + P_d(u'') \frac{\partial}{\partial \alpha_n} P_d^*(u + u'') \right) \\ &= \frac{1}{N^2} \sum_{cc} \sum_{u'' \in \mathcal{U}} E_{cc}(u'') E_{cc}(u + u'') [i\Phi_n(u'') P_d(u'') P_d^*(u + u'') - i\Phi(u + u'') P_d(u'') P_d^*(u + u'')] \\ &= \frac{1}{N^2} \sum_{cc} \sum_{u'' \in \mathcal{U}} i\Phi_n(u'') E_{cc}(u'') E_{cc}(u + u'') P_d(u'') P_d^*(u + u'') \dots \\ &\dots - \frac{1}{N^2} \sum_{cc} \sum_{u' \in \mathcal{U}} i\Phi_n(u') E_{cc}(u') E_{cc}(u' - u) P_d(u') P_d^*(u' - u) \\ &= \frac{i}{N^2} \sum_{cc} \sum_{u' \in \mathcal{U}} \Phi_n(u') E_{cc}(u') [E_{cc}(u + u') P_d(u') P_d^*(u + u') - E_{cc}(u' - u) P_d^*(u') P_d(u' - u)] \end{aligned}$$

where between the second and third step we have performed a change of variables $u' = u + u''$. We can now substitute the result into eq. (4-13) and obtain:

$$\begin{aligned} \frac{\partial}{\partial \alpha_n} L_M &= \sum_{u \in \mathcal{U}} \sum_{d=1}^m Z_d(u) \frac{i}{N^2} \sum_{cc} \sum_{u' \in \mathcal{U}} \Phi_n(u') E_{cc}(u') [E_{cc}(u + u') P_d(u') P_d^*(u + u') \dots \\ &\dots - E_{cc}(u' - u) P_d^*(u') P_d(u' - u)] + c.c. \\ &= \left[\frac{i}{N^2} \sum_{cc} \sum_{u' \in \mathcal{U}} \Phi_n(u') E_{cc}(u') \sum_{d=1}^m P_d(u') \sum_{u \in \mathcal{U}} Z_d(u) P_d^*(u + u') E_{cc}(u + u') \right] + c.c \dots \\ &\dots - \left[\frac{i}{N^2} \sum_{cc} \sum_{u' \in \mathcal{U}} \Phi_n(u') E_{cc}(u') \sum_{d=1}^m P_d^*(u') \sum_{u \in \mathcal{U}} Z_d(u) P_d(u' - u) E_{cc}(u' - u) \right] + c.c \end{aligned}$$

Let us now focus on the first term in square brackets of the equation above. Thanks to the Hermitian property of Z_d (i.e. $Z_d(u) = Z_d^*(-u)$) and a change of variables $u'' = -u$, it can be rewritten as:

$$\frac{i}{N^2} \sum_{cc} \sum_{u' \in \mathcal{U}} \Phi_n(u') E_{cc}(u') \sum_{d=1}^m P_d(u') \sum_{u'' \in \mathcal{U}} Z_d^*(u'') P_d^*(u' - u'') E_{cc}(u' - u'')$$

Which clearly shows that it is the complex conjugate of the second term in squared brackets. We can therefore rewrite the derivative of the co-log-likelihood as:

$$\begin{aligned}\frac{\partial}{\partial \alpha_n} L_M &= \frac{2i}{N^2} \sum_{cc} \sum_{u' \in \mathcal{U}} \Phi_n(u') E_{cc}(u') \sum_{d=1}^m P_d(u') \sum_{u \in \mathcal{U}} Z_d^*(u) P_d^*(u' - u) E_{cc}(u' - u) + c.c. \\ &= -\frac{4}{N^2} \sum_{cc} \sum_{u' \in \mathcal{U}} \Phi_n(u') E_{cc}(u') \operatorname{Im} \left\{ \sum_{d=1}^m P_d(u') (Z_d^* \circledast (P_d^* E_{cc}))(u') \right\}\end{aligned}$$

where \circledast represents a discrete convolution and the operator $\operatorname{Im}\{\}$ takes the imaginary part. If we now we had delta functions as basis functions, the gradient would simplify to:

$$\frac{\partial}{\partial \alpha_n} L_M = -\frac{4}{N^2} \sum_{cc} E_{cc}(u_n) \operatorname{Im} \left\{ \sum_{d=1}^m P_d(u_n) (Z_d^* \circledast (P_d^* E_{cc}))(u_n) \right\} \quad (\text{C-9})$$

Bibliography

- [1] M. J. Booth, “Adaptive optical microscopy: The ongoing quest for a perfect image,” *Light: Science and Applications*, vol. 3, apr 2014.
- [2] M. R. Banham and A. K. Katsaggelos, “Digital image restoration,” *IEEE Signal Processing Magazine*, vol. 14, no. 2, pp. 24–41, 1997.
- [3] D. Baddeley and J. Bewersdorf, “Biological Insight from Super-Resolution Microscopy: What We Can Learn from Localization-Based Images,” *Annual Review of Biochemistry*, vol. 87, pp. 965–989, jun 2018.
- [4] S. T. Hess, T. P. Girirajan, and M. D. Mason, “Ultra-high resolution imaging by fluorescence photoactivation localization microscopy,” *Biophysical Journal*, vol. 91, no. 11, pp. 4258–4272, 2006.
- [5] X. Tao, B. Fernandez, O. Azucena, M. Fu, D. Garcia, Y. Zuo, D. C. Chen, and J. Kubby, “Adaptive optics confocal microscopy using direct wavefront sensing,” *Optics Letters*, vol. 36, p. 1062, apr 2011.
- [6] R. W. Gerchberg and W. O. Saxton, “A Practical Algorithm for the Determination of Phase from Image and Diffraction Plane Pictures,” *ppl. Opt*, vol. 35, no. 2, pp. 237–246, 1972.
- [7] B. Richards and E. Wolf, “Electromagnetic diffraction in optical systems, II. Structure of the image field in an aplanatic system,” *Proceedings of the Royal Society of London. Series A. Mathematical and Physical Sciences*, vol. 253, pp. 358–379, dec 1959.
- [8] L. Ciocci, J. M. Simon, and R. M. Echarri, “Diffraction in high numerical aperture systems: polarization effects,” *Journal of Optics J. Opt*, vol. 12, p. 6, 2010.
- [9] H. T. Nguyen, O. Soloviev, and M. Verhaegen, “Phase retrieval based on the vectorial model of point spread function,” *Journal of the Optical Society of America A*, vol. 37, p. 16, jan 2020.

- [10] B. Ferdman, E. Nehme, L. E. Weiss, R. Orange, O. Alalouf, and Y. Shechtman, “VIPR: Vectorial Implementation of Phase Retrieval for fast and accurate microscopic pixel-wise pupil estimation,” *bioRxiv*, 2020.
- [11] P. Kner, L. Winoto, D. A. Agard, and J. W. Sedat, “Closed loop adaptive optics for microscopy without a wavefront sensor,” in *Three-Dimensional and Multidimensional Microscopy: Image Acquisition and Processing XVII*, vol. 7570, p. 757006, SPIE, feb 2010.
- [12] B. M. Hanser, M. G. Gustafsson, D. A. Agard, and J. W. Sedat, “Phase-retrieved pupil functions in wide-field fluorescence microscopy,” *Journal of Microscopy*, vol. 216, pp. 32–48, oct 2004.
- [13] N. Ji, “Adaptive optical fluorescence microscopy,” *Nature Methods*, vol. 14, no. 4, pp. 374–380, 2017.
- [14] R. A. Gonsalves, “Phase Retrieval And Diversity In Adaptive Optics,” *Optical Engineering*, vol. 21, oct 1982.
- [15] R. G. Paxman, T. J. Schulz, and J. R. Fienup, “Joint estimation of object and aberrations by using phase diversity,” *Journal of the Optical Society of America A*, vol. 9, p. 1072, jul 1992.
- [16] J. H. Seldin and R. G. Paxman, “Joint estimation of amplitude and phase from phase-diversity data,” in *Optics InfoBase Conference Papers*, Optical Society of America, 2005.
- [17] R. L. Kendrick, D. S. Acton, and A. L. Duncan, “Phase-diversity wave-front sensor for imaging systems,” *Applied Optics*, vol. 33, p. 6533, sep 1994.
- [18] J. W. Goodman, *Introduction to Fourier optics*. Roberts & Co, 2005.
- [19] K. R. Spring, T. J. Fellers, and M. W. Davidson, “Olympus FluoView Resource Center: Resolution and Contrast in Confocal Microscopy.”
- [20] E. Wolf, “Electromagnetic diffraction in optical systems - I. An integral representation of the image field,” *Proceedings of the Royal Society of London. Series A. Mathematical and Physical Sciences*, vol. 253, pp. 349–357, dec 1959.
- [21] J. D. Jackson, *Classical Electrodynamics 2ed (1975)*. Wiley, 1975.
- [22] J. Kim, Y. Wang, and X. Zhang, “Calculation of vectorial diffraction in optical systems,” *Journal of the Optical Society of America A*, vol. 35, p. 526, apr 2018.
- [23] M. Mansuripur, *Classical optics and its applications*, vol. 9780521881. Cambridge University Press, 2nd ed., jan 2009.
- [24] M. Mansuripur, “Distribution of light at and near the focus of high-numerical-aperture objectives,” *Journal of the Optical Society of America A*, vol. 3, no. 12, p. 2086, 1986.
- [25] D. F. J. Arago and A. J. Fresnel, “On the action of rays of polarized light upon each other,” *Ann. Chim. Phys.*, vol. 3, p. 288, 1819.

-
- [26] J. R. Fienup, “Phase retrieval algorithms: a comparison,” *Applied Optics*, vol. 21, p. 2758, aug 1982.
- [27] Y. Shechtman, Y. C. Eldar, O. Cohen, H. N. Chapman, J. Miao, and M. Segev, “Phase Retrieval with Application to Optical Imaging: A contemporary overview,” may 2015.
- [28] J. R. Fienup, “Reconstruction of an object from the modulus of its Fourier transform,” *Optics Letters*, vol. 3, p. 27, jul 1978.
- [29] L.-H. Yeh, J. Dong, J. Zhong, L. Tian, M. Chen, G. Tang, M. Soltanolkotabi, and L. Waller, “Experimental robustness of Fourier ptychography phase retrieval algorithms,” *Optics Express*, vol. 23, p. 33214, dec 2015.
- [30] R. P. Millane, “Phase retrieval in crystallography and optics,” *Journal of the Optical Society of America A*, vol. 7, p. 394, mar 1990.
- [31] B. M. Hanser, M. G. L. Gustafsson, D. A. Agard, and J. W. Sedat, “Phase retrieval for high-numerical-aperture optical systems,” *Optics Letters*, vol. 28, p. 801, may 2003.
- [32] F. Soulez, É. Thiébaut, A. Schutz, A. Ferrari, F. Courbin, and M. Unser, “Proximity operators for phase retrieval,” *Applied Optics*, vol. 55, p. 7412, sep 2016.
- [33] L. M. Mugnier, A. Blanc, and J. Idier, “Phase Diversity: A Technique for Wave-Front Sensing and for Diffraction-Limited Imaging,” jan 2006.
- [34] R. A. Gonsalves and R. Chidlaw, “Wavefront sensing by phase retrieval.,” *Applications of digital image processing III*, pp. 32–39, 1979.
- [35] R. K. Pina and R. C. Puetter, “Incorporation of Spatial Information in Bayesian Image Reconstruction: The Maximum Residual Likelihood Criterion,” *Publications of the Astronomical Society of the Pacific*, vol. 104, p. 1096, 1992.
- [36] W. H. Press, S. A. Teukolsky, W. T. Vetterling, and B. P. Flannery, *Numerical Recipes in C*. e Press Syndicate of the University of Cambridge, 2nd ed., 1992.
- [37] D. Dravins, L. Lindegren, E. Mezey, and A. T. Young, “Atmospheric Intensity Scintillation of Stars, I. Statistical Distributions and Temporal Properties,” *Publications of the Astronomical Society of the Pacific*, vol. 109, p. 173, 1997.
- [38] P. Kner, “Phase diversity for three-dimensional imaging,” *Journal of the Optical Society of America A*, vol. 30, p. 1980, oct 2013.
- [39] S. M. Jefferies, M. Lloyd-Hart, E. K. Hege, and J. Georges, “Sensing wave-front amplitude and phase with phase diversity,” *Applied Optics*, vol. 41, no. 11, p. 2095, 2002.

Glossary

List of Acronyms

DCSC	Delft Center for Systems and Control
NA	Numerical Aperture
PSF	Point Spread Function
CDI	Coherent Diffraction Imaging
OTF	Optical Transfer Function
GS	Gerchberg and Saxton
HIO	Hybrid Input-Output
VAM	Vectorial Alternating Minimization
RMS	Root Mean Square
SNR	Signal to Noise Ratio
SSIM	Structural Similarity Index Measure
DM	Deformable Mirror

List of Symbols

\circledast	Convolution
\hat{x}	Unit Vector in the Direction of the x Axis
\mathcal{F}	Fourier Transform
$\nabla \cdot$	Divergence Operator
$\nabla \times$	Curl Operator
\times	Cross Product
H_1^*	Complex conjugate of H_1
$Im\{\}$	Operator taking the imaginary part of a complex number
$Re\{\}$	Operator taking the real part of a complex number